

Generating high-efficiency swimming kinematics using hydrodynamic eigenmode decomposition

A. S. M. Smyth,¹ A. M. Young,² and L. Di Mare³

¹*Department of Engineering Science, University of Oxford, Parks Road, Oxford OX1 3PJ, UK*

²*Department of Mechanical Engineering, University of Bath, Claverton Down, Bath BA2 7AY, UK*

³*Department of Engineering Science, University of Oxford, Parks Road, Oxford OX1 3PJ, UK*

(*Electronic mail: amanda.smyth@eng.ox.ac.uk)

(Dated: 9 August 2023)

This paper explores the use of hydrodynamic eigenmode decomposition as a means of generating optimal swimming kinematics of slender three-dimensional bodies. The eigenvectors of the unsteady hydrodynamic system are used as basis functions for the response to external forcing, such as perturbations generated by the deformation of the body. Exploiting the orthogonality of the modes, we show that swimming according to a single appropriately selected hydrodynamic eigenmode results in high-efficiency swimming. To demonstrate this result, we use an inviscid three-dimensional vortex lattice model to investigate the hydrodynamic eigenmodes of a selection of geometries. We find that for all of the body geometries tested, hydrodynamic efficiency far exceeding that of pure heaving or pitching can be achieved. All eigenmodes tested produce high-efficiency motion, as long as the beat frequency is higher than the mode's "cut-in" frequency for thrust generation. The eigenmodes show qualitative similarity to swimming patterns observed in nature, and also correspond well to the existing classifications of undulatory and oscillatory swimming. This study demonstrates that hydrodynamic eigenmode analysis can generate high-efficiency swimming kinematics based only on information about the body and wake geometry, and as such this method has significant potential for further development and application to autonomous underwater vehicle design.

I. INTRODUCTION

A. Motivation for study

Achieving the high-efficiency swimming motion observed in marine animals is one of the primary challenges in the field of bio-mimicking and bio-inspired underwater robotics. Current state-of-the-art autonomous underwater vehicles (AUVs) are generally either torpedo-shaped designs optimised for high-speed cruising, with low manoeuvrability, or box-shaped designs with little consideration for hydrodynamic efficiency. However, the development of more advanced bio-inspired vehicles is being made possible through advances such as soft robotics, flexible membranes, and improved understanding of the features of high-efficiency swimming. Historically, research into swimming efficiency has focused on the optimum combination of pitching and heaving motion for the propulsive efficiency of flapping plates of various shapes^{1–5}, as well as features of the wake structure associated with high thrust production^{3,4,6–9}. The importance of body flexibility in generating high-efficiency propulsive motion has also been demonstrated in several studies^{10–13}. Progress in these fields has given rise to highly advanced bio-inspired robots, a notable example being the "tunabot" presented in White et al. (2021)¹⁴.

Despite these recent advances in the understanding of efficient swimming, significant difficulties are often encountered in reproducing the swimming motions seen in nature, and in achieving the associated high propulsive efficiencies. Pure flapping, pitching or heaving motion have repeatedly been shown to be insufficient to fully characterise optimal

motion^{12,15}. Also, while the tail fin is generally considered to be the primary generator of thrust^{16,17}, movement of the rest of the body is often crucial to reduce "recoil" motion which would otherwise lead to substantial reductions in swimming efficiency¹⁸. The characterisation and the identification of universal features of high-efficiency swimming kinematics remains challenging. As such, determining the optimal swimming kinematics for a given body geometry often requires either detailed measurements of body motions of real fish¹⁹, or repeated trial-and-error.

This work aims to demonstrate a model able to generate high-efficiency swimming kinematics for a given geometry, through the use of hydrodynamic eigenmodes. As will be demonstrated in Section II, these modes define the set of mutually independent responses of a body to hydrodynamic forcing. The circulation of the lifting surface can be represented as a weighted sum of such eigenmodes. Using this principle, it is possible to demonstrate that the most efficient swimming can be achieved through a body motion defined by a single hydrodynamic eigenmode. Based on this result, which will be demonstrated in section II, this paper addresses the following questions:

1. What are the propulsive properties of the eigenmodes?
2. How does swimmer geometry affect the eigenmodes?
3. Are any known features of efficient swimming found in the eigenmodes?

To answer these questions, this study uses an inviscid frequency-domain vortex lattice model (VLM – outlined in section III) to find the hydrodynamic eigenmodes of various

3D geometries and evaluate their propulsive properties. While the VLM used in this paper relies on the simplified assumptions of small-amplitude inviscid flow, the outcomes form a theoretical basis to the hydrodynamic eigenmode problem, which allows for extension to large-amplitude viscous flows in future studies.

B. Background: features of efficient swimming

This section contains a summary review of previous work on bio-inspired swimming, for the purpose of establishing the known features of efficient propulsion and the common methods used for characterisation of swimming motion. For a more complete overview of the history of swimming propulsion research, readers are referred to Sfakiotakis et al. (1999)²⁰ for historical context, and to Smits (2019)¹⁷ for a more recent perspective.

Early research into swimming motion utilised inviscid slender-body theory or lifting surface theory for analysis of the physics of swimming^{18,21–23}. Slender-body theory divides the geometry into independent chordwise sections, and considers only added mass forces. Despite these simplifications, the theory was able to illustrate several features of efficient swimming motion, such as showing that virtually all thrust is generated at or near the trailing edge; this finding was later verified experimentally¹⁷. The apparent importance of the tail has meant that the characteristic velocity for swimming efficiency is generally taken to be the lateral speed of the trailing edge. This choice of characteristic velocity is supported by experimental results, such as in the studies of lamprey swimming by Hultmark et al. (2007)²⁴ and Leftwich and Smits (2011)²⁵, who demonstrated a close connection between tail motion and thrust production. The shape and movements of the tail fin have therefore been assumed to be of primary importance for thrust generation and have been the focus of most work. Numerous studies of heaving and pitching airfoils of various shapes, in 2D^{4,26,27} and 3D^{6,7,28–31}, have been carried out in attempts to characterise the kinematic and geometric features of efficient tail fins. The importance of the tail fin lateral velocity has also been used to explain why the amplitude of motion of marine animals tends to follow an exponential increase from leading edge to trailing edge^{23,24,32}.

However, the characteristics of high-efficiency motion kinematics are more complex than simply high-speed movement of the trailing edge³³. Pure pitch or heave of the tail fin is not an efficient way of generating thrust; rather, a combination of heave and pitch^{12,34}, or travelling wave motion involving the whole body²², have been shown to produce more efficient swimming than pure pitch or heave. Dramatic changes to swimming dynamics have been observed when varying the body flexibility, with local peaks in swimming speeds or propulsive efficiency observed with varying body flexibility^{11,33,35}.

Another reason for the importance of whole-body swimming motion is the avoidance of “recoil”, identified by Lighthill (1960)¹⁸ as a consequence of the conservation of lateral and angular momentum. Significant recoil when swim-

ming leads to additional lateral or angular body motion to satisfy momentum conservation, and so causes an overall reduction in thrust and swimming efficiency³⁶. Lighthill demonstrated that recoil can be reduced when swimming by using a travelling wave motion¹⁸: if there is both a positive and negative wave phase present on the body during the motion then the lateral and angular moments are cancelled out (e.g. in eel swimming).

The travelling wave swimming motion exhibited by eels has historically been labelled “anguilliform” locomotion. Some other classical categories of swimming locomotion are carangiform (exhibited by e.g. mackerel), sub-carangiform (e.g. trout) and thunniform (e.g. tuna, sharks) – for an overview of these notations, see Sfakiotakis et al. (1999)²⁰. However, a different classification has been proposed by Webb and Blake (1985)³⁷, who suggested division into “undulatory” and “oscillatory” swimmers. According to the characterisation by Smits (2019)¹⁷, the former are characterised as swimming with a travelling wavelength shorter than the body (e.g. eels), and the latter as swimming with a wavelength longer than the body (e.g. tuna). This categorisation will be shown to be appropriate for the characterisation of the hydrodynamic eigenmodes studied in this paper, and as such the undulatory and oscillatory motion classifications will be used throughout this work.

An issue with oscillatory swimming is the potential for significant recoil motion. Lighthill proposed that this issue is overcome in fish through the use of a high-mass main body with a narrowing rear section, before extending again into the lightweight tail fin²¹. This manipulation of the centre of mass minimises the recoil motion, despite the absence of a matching pair of positive- and negative-phase waves on the body in oscillatory swimming. As discussed above, undulatory swimmers are considered to have inherently low recoil.

The performance of swimmers has historically been measured assuming harmonic motion, by calculating the cycle-average thrust generated (\bar{T}) and comparing it with the cycle-average power required to produce the motion (\bar{P}). The swimming (or Froude) efficiency is then given by:

$$\eta = \frac{U\bar{T}}{\bar{P}} \quad (1)$$

where U is the resulting swimming velocity obtained after overcoming the drag of the body. In the majority of past analyses the swimming velocity U has been held constant, for ease of computation. This approach is also taken in the present study. However, there are some notable examples of past studies that used models where U is an output variable^{19,35,38}, which is arguably more appropriate for swimming motion. The model developed by Moored (2018)³⁸ was subsequently used in a number of studies seeking to identify the scaling parameters and characteristic non-dimensional groups determining swimming performance^{28,39}. These studies verified previous observations that the reduced frequency and the Strouhal number are two key parameters determining propulsive efficiency of tail fins, in this paper respectively defined as:

$$\kappa = \frac{2\pi fc}{U} \quad (2)$$

$$St = \frac{2af}{U} = \frac{\kappa a}{\pi c} \quad (3)$$

where c represents chord length, f the tail beat frequency and a the maximum amplitude of movement.

In observations of a wide range of swimmers in nature, Triantafyllou et al. (1993)⁴⁰ showed that they all tended to swim within the range of $St = 0.2 - 0.5$. They further showed that a heaving and pitching foil exhibited an efficiency peak in this range. The reduced frequency of propulsive swimming can generally not be considered quasi-steady ($\kappa > 0.1$ for most swimmers), with the exception of very large mammals⁴¹. Van Buren et al. (2019)³⁴ showed that the propulsive efficiency of an oscillating plate exhibits a peak in the range $\kappa = 1.4\pi - 2\pi$, while Floryan et al. (2017)⁴² observed the efficiency of different heaving plates to plateau for $\kappa > 1.5\pi$. Dong et al. (2006)⁶ also observed peaks in the hydrodynamic efficiency of oscillating low-aspect-ratio plates; the reduced frequency at which the peak occurred was found to increase with the Strouhal number.

In this paper the hydrodynamic eigenmodes of a selection of geometries will be examined, to demonstrate how they correspond to the features and categories of efficient swimming outlined in this section. But first the method of eigenmode decomposition will be outlined in Section II, and the details of the vortex lattice model introduced in section III.

II. EIGENMODE DECOMPOSITION

A. Theory

This study focuses on the hydrodynamic eigenmodes of lifting surfaces. By contrast, the role of the structural eigenmodes in determining the response of flexible foils and membranes to heaving or pitching actuation has been investigated in several past studies. For example, Mavroyiakoumou and Alben (2021)⁴³ studied membrane stability for the prediction of flutter, Quinn et al. (2014)¹¹ experimentally studied the propulsive efficiency of panels with varying flexibility, and Floryan and Rowley (2018)¹³ used a linear inviscid model to study the effects of flexibility on propulsive performance of swimmers. In these past studies, either the structural eigenmodes of the body, or the eigenmodes of the coupled fluid-structure system were considered. The present study focuses on the hydrodynamic eigenmodes only, and does not consider body flexibility or any presupposed forcing actuation. The purpose is to identify optimal swimming kinematics from a purely hydrodynamic perspective, by maximising the Froude efficiency (Equation 1). Having developed a method for generating swimming kinematics that maximise the Froude efficiency in the present paper, the role of body flexibility in achieving the desired kinematics will be explored in future studies.

The eigenmode decomposition method used in this paper is based on that developed by Hall et al.⁴⁴⁻⁴⁶ for the purpose of creating reduced order models of unsteady airfoil response. The method can be applied to any linearized system for fluid modelling, including field-discretized CFD solvers⁴⁴ and boundary-element solvers⁴⁵.

Consider a flow-surface interaction system with a governing equation of the form:

$$\mathbf{A}\mathbf{\Gamma} = \mathbf{u} = \mathbf{B}\mathbf{h} \quad (4)$$

where \mathbf{u} is the vector of surface-normal velocity, $\mathbf{\Gamma}$ is the vector defining the circulation distribution of the lifting surface, and \mathbf{A} is the matrix transform between surface circulation and surface-normal velocity induced by the lifting surface. To translate this to body motion, \mathbf{B} transforms the body displacement vector \mathbf{h} into surface-normal velocity. As long as the hydrodynamic system is expressed in the form given in Equation 4, the eigenmode analysis given below is applicable. The present work uses a simple inviscid vortex lattice model, however more advanced viscous or large-amplitude models could also be used. The details of matrices \mathbf{A} and \mathbf{B} as used in this paper are given in section III.

The basic principle of the eigenmode decomposition used by Hall et al.⁴⁴⁻⁴⁶ is that the vector defining the surface circulation $\mathbf{\Gamma}$ can be reconstructed as a sum of the right eigenvectors of the aero/hydrodynamic system:

$$\mathbf{\Gamma} = \mathbf{R}\mathbf{\alpha} = \sum_k \mathbf{v}_{Rk} \alpha_k \quad (5)$$

Here \mathbf{R} represents the matrix of right eigenvectors obtained from the generalised eigenvalue problem using matrices \mathbf{A} and \mathbf{B} in Equation 4, with \mathbf{v}_{Rk} indicating the right eigenvector located in the k 'th column. The vector $\mathbf{\alpha}$ represents a weight function, the exact form of which will depend on the aero/hydrodynamic model. This reconstruction corresponds to using the eigenvectors as a linear basis for representing the surface circulation. Note that the circulation is related to the added mass force through the time derivative $d\mathbf{\Gamma}/dt$, which for a harmonic system (as used in this study) is equal to $j\omega\mathbf{\Gamma}$ where ω is the harmonic frequency in radians per second and $j = \sqrt{-1}$. Thus, the eigenmodes also implicitly operate as a basis for the added mass.

Substituting the expression in Equation 5 into Equation 4, the following rearrangement of terms is possible:

$$\mathbf{A}\mathbf{R}\mathbf{\alpha} = \mathbf{B}\mathbf{h} \quad (6)$$

$$\mathbf{L}\mathbf{A}\mathbf{R}\mathbf{\alpha} = \mathbf{L}\mathbf{B}\mathbf{h} \quad (7)$$

Here \mathbf{L} represents the Hermitian of the matrix of left eigenvectors obtained from the generalised eigenvalue problem. Noting the following property of the eigenmodes (if correctly scaled), if $\mathbf{\Lambda}$ is the diagonal matrix of eigenvalues, then:

$$\mathbf{L}\mathbf{A}\mathbf{R} = \mathbf{A} \quad (8)$$

This expression can then be inserted into Eq. 7, yielding:

$$\mathbf{A}\boldsymbol{\alpha} = \mathbf{L}\mathbf{B}\mathbf{h} \quad (9)$$

$$\boldsymbol{\alpha} = \mathbf{A}^{-1}\mathbf{L}\mathbf{B}\mathbf{h} \quad (10)$$

As such, the circulatory (and, by implication, added mass) response of the hydrodynamic system to any arbitrary perturbation can be obtained from a weighted sum of the right eigenvectors, where the weights $\boldsymbol{\alpha}$ are obtained using Equation 10 given knowledge of the perturbation vector \mathbf{u} (external flow perturbation) or \mathbf{h} (body motion). This effectively gives the solution for $\boldsymbol{\Gamma}$ in the form of a Green's function.

B. Generating optimal swimming kinematics from the eigenvectors

Here we will argue that optimal propulsive swimming kinematics are achieved by choosing \mathbf{h} such that all entries in the weight function vector $\boldsymbol{\alpha}$ are zero, except for one single entry corresponding to an appropriately chosen eigenvector. We define “optimum” swimming kinematics as the motion that maximises the Froude efficiency given in Equation 1. Considering that the left and right eigenvectors are orthogonal (such that $\mathbf{L}\mathbf{B}\mathbf{R} = \mathbf{I}$), we see that the vector $\boldsymbol{\alpha}$ in Equation 10 is zero at all but one entry if the body motion \mathbf{h} is parallel to a single right eigenvector:

$$\mathbf{h} = \beta \mathbf{v}_{Rk} \quad (11)$$

where k indicates the mode number of interest and β is a scalar. An argument for why this results in optimal body kinematics will now be given for the simplified case of high-frequency motion dominated by added mass forces. An extended analysis that includes circulatory forces is demonstrated in Appendix A.

In the simplified case of high-frequency harmonic motion, the local pressure on a slender body in the (x,y) -plane can be approximated from the added mass. We express time-varying harmonic properties in terms of Fourier components (e.g. $\Gamma(x,y,t) = \hat{\Gamma}(x,y)e^{j\omega t}$), such that the surface pressure from added mass can be written (with subscript m pertaining to the added mass components of pressure and force):

$$p_m(x,y,t) = \rho \frac{\partial}{\partial t} \int_0^x \gamma(x,y,t) dx = j\omega\rho\Gamma(x,y,t) \quad (12)$$

where γ is the circulation per unit span and chord and $j = \sqrt{-1}$. The (x,y) notation indicates a surface distribution. The resulting force acts along the surface normal vector, which for small-amplitude harmonic motion can be approximated as

$$\mathbf{n}(x,y,t) = \begin{bmatrix} 0 \\ 0 \\ 1 \end{bmatrix} + e^{j\omega t} \begin{bmatrix} \hat{a} \\ \hat{b} \\ 0 \end{bmatrix} (x,y) \quad (13)$$

where $\hat{a}(x,y)$ and $\hat{b}(x,y)$ are the amplitudes of the harmonic variations of the x - and y - components of the local surface normal. If the surface displacement vector $\mathbf{h}(x,y,t)$ is given by

$$\mathbf{h}(x,y,t) = e^{j\omega t} \begin{bmatrix} 0 \\ 0 \\ \hat{h} \end{bmatrix} (x,y) \quad (14)$$

then $\hat{a}(x,y)$ and $\hat{b}(x,y)$ are related to the surface displacement as follows:

$$\begin{bmatrix} \hat{a} \\ \hat{b} \end{bmatrix} (x,y) \approx - \begin{bmatrix} \frac{\partial \hat{h}}{\partial x} \\ \frac{\partial \hat{h}}{\partial y} \end{bmatrix} (x,y) = -\frac{1}{c} \begin{bmatrix} \frac{\partial \hat{h}}{\partial s} \\ \frac{\partial \hat{h}}{\partial r} \end{bmatrix} (x,y) \quad (15)$$

where s and r are non-dimensional streamwise and spanwise coordinates on the surface and c is the chord length. For slender bodies we can use $s = x/c$ and $r = y/c$. The instantaneous total thrust force from added mass is then

$$\begin{aligned} T_m &= \int_S -\text{Re}[p_m] \text{Re}[\mathbf{n} \cdot \mathbf{i}] dS \\ &= \frac{\omega\rho}{c} \int_S \text{Re}[j\Gamma(x,y,t)] \text{Re}\left[\frac{\partial h(x,y,t)}{\partial s}\right] dS \end{aligned} \quad (16)$$

where S is the surface area and $(\mathbf{i} \ \mathbf{j} \ \mathbf{k})$ are the unit vectors for the (x,y,z) directions. It can further be demonstrated that the resulting cycle-average thrust from added mass is given by

$$\bar{T}_m = -\frac{\rho\omega}{2c} \int_S \text{Im}[\hat{\Gamma}^*(x,y) \frac{\partial \hat{h}(x,y)}{\partial s}] dS \quad (17)$$

where the superscript $*$ indicates the complex conjugate. The instantaneous power required to produce the body motion is defined as the inner product of the body force with the transverse body velocity, which for the added mass is given by

$$\begin{aligned} P_m &= \int_S \text{Re}[p_m(x,y,t)(\mathbf{n} \cdot \mathbf{k})] \text{Re}\left[\frac{\partial \mathbf{h}(x,y,t)}{\partial t} \cdot \mathbf{k}\right] dS \\ &= \rho\omega^2 \int_S \text{Re}[j\Gamma(x,y,t)] \text{Re}[jh(x,y,t)] dS \end{aligned} \quad (18)$$

The cycle-average is then given by

$$\bar{P}_m = \frac{\rho\omega^2}{2} \int_S \text{Re}[\hat{\Gamma}^*(x,y) \hat{h}(x,y)] dS \quad (19)$$

Following the definition in Equation 1, the following expression for efficiency in terms of the added mass forces is obtained:

$$\eta_m = \frac{U \bar{T}_m}{\bar{P}_m} = -\frac{1}{\kappa} \frac{\int_S \text{Im} \left[\hat{\Gamma}^*(x, y) \frac{\partial \hat{h}(x, y)}{\partial s} \right] dS}{\int_S \text{Re} [\hat{\Gamma}^*(x, y) \hat{h}(x, y)] dS} \quad (20)$$

It is notable that for the case of uniform travelling sinusoidal wave motion in 2D, $\frac{\partial \hat{h}}{\partial s} = -j\kappa \hat{h}$ (resulting in $\eta = 1$) corresponds to a travelling wave speed equal to the reduced frequency, which Wu (1961)²² demonstrated has a Froude efficiency of 1. Thus the present analysis agrees with Wu's results.

At this point we can approximate Equation 20 for a discrete surface distribution with N cells, allowing us to express the surface distribution of properties as column vectors. The Froude efficiency is then approximated as:

$$\eta_m \approx -\frac{1}{\kappa} \frac{\sum_k \text{Im} [\hat{\Gamma}_k^* (\frac{\partial \hat{h}}{\partial s})_k]}{\sum_k \text{Re} [\hat{\Gamma}_k^* \hat{h}_k]} \quad (21)$$

We can now express the circulation vector $\hat{\Gamma}$ as a sum of eigenvectors according to Equation 5. We also express the arbitrary displacement vector \hat{h} as a sum of the eigenvectors, such that

$$\hat{h} = R\beta \quad (22)$$

where β is the vector of weight functions required to produce the desired perturbation vector. The vector β can be chosen freely, to give any arbitrary surface motion. Thus we obtain:

$$\eta_m \approx -\frac{1}{\kappa} \frac{\sum_k \text{Im} [(R\alpha)_k^* (\frac{\partial R}{\partial s} \beta)_k]}{\sum_k \text{Re} [(R\alpha)_k^* (R\beta)_k]} \quad (23)$$

Without loss of generality, we can expand the differential $(\frac{\partial R}{\partial s})$ as follows:

$$\frac{\partial R}{\partial s} = -j\kappa(R - R\epsilon) \quad (24)$$

where the matrix ϵ represents the deviation of the differential $\frac{\partial R}{\partial s}$ from $-j\kappa R$. This allows for further simplification of Equation 23:

$$\eta_m \approx 1 - \frac{\sum_k \text{Im} [(R\alpha)_k^* (jR\epsilon\beta)_k]}{\sum_k \text{Re} [(R\alpha)_k^* (R\beta)_k]} \quad (25)$$

Thus the propulsive efficiency is fully determined by the matrix ϵ , which is an $[N \times N]$ matrix where N is the number of columns in the matrix of eigenvectors R . It can be obtained as follows (noting that, if the eigenvectors are scaled appropriately, $LB R$ produces the identity matrix I):

$$\epsilon = I + \frac{1}{jk} LB \frac{\partial R}{\partial s} \quad (26)$$

Equation 25 shows that the propulsive efficiency of any arbitrary harmonic body motion will depend on ϵ , the entries of which will appear as a sum in the numerator of the fraction in Equation 25. In order to maximise the Froude efficiency, the fraction in Equation 25 should be minimised, through an appropriate choice of the weight function β which determines the body motion.

One way to obtain the body motion vector h resulting in the highest efficiency is to choose β to be a vector in the null space of ϵ . However, in the present study the ϵ -matrices evaluated generally have full rank. An alternative method is to choose β to be zero everywhere except for the single entry corresponding to the smallest diagonal value of ϵ . In this scenario only this single entry from the diagonal of ϵ will appear in Equation 25 since the rest will be multiplied by the zero-entries in β . The single entry of ϵ thus determines the overall efficiency. By contrast, if β is zero everywhere except at M entries, then $M \times M$ terms from ϵ will contribute to the numerator in Equation 25, including both diagonal entries and off-diagonal entries. The sum of all these $M \times M$ entries will then determine the efficiency. As such, in the absence of a null space of ϵ , adding more entries in β will always be detrimental to the overall efficiency. From Equation 22, if β is nonzero only at a single entry the body motion is given by the corresponding right eigenvector (as in Equation 11). The analysis thus suggests that Froude efficiency is maximised by swimming according to a single appropriately chosen eigenvector.

An illustration of the effects of ϵ on propulsive efficiency is shown in Figure 1. The results are obtained using the vortex lattice model outlined in Section III, for a square plate discretized on a 10×10 grid for $\kappa = 10$. The grey bars in Figure 1a give the propulsive efficiencies of all eigenmodes that produce positive cycle-average thrust \bar{T}_m . Light grey bars represent efficiency from added mass forces only (η_m), while dark grey bars represent efficiency including both added mass and circulatory forces (η). Overlaid as a line plot is the negative imaginary component of the diagonal entry of ϵ , which can be seen to correspond inversely to η_m as expected.

When considering the full propulsive efficiency η , ϵ is not a good indicator of efficiency for modes 1-5 in Figure 1a since these have significant contributions from circulatory forces. As is demonstrated in Appendix A, it is not possible to express η as a function of a single parameter as it is for η_m in Equation 25. However, we demonstrate that the optimum is still to swim according to a single eigenvector, rather than a combination of multiple eigenvectors. This is further illustrated in Figure 1b, showing the ϵ -matrix corresponding to the modes in Figure 1a as a heat map. There are a number of off-diagonal entries with comparable magnitudes to the diagonal entries, further showing the benefit of that having only one non-zero entry in β . Because ϵ is not always a good predictor of η , and because we have demonstrated that single-eigenvector solutions are optimal, in the remainder of this paper we identify high-efficiency body motion by directly evaluating the efficiency of every thrust-producing mode, including both added mass and circulatory forces. This process will be demonstrated in Section IV, and the vortex lattice model used to produce the results is outlined in Section III.

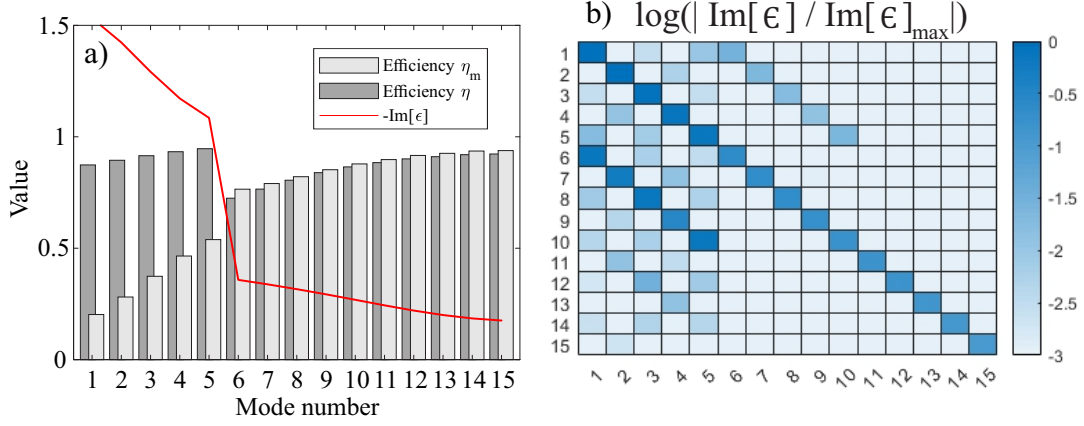


FIG. 1. a) The efficiency of all thrust-producing eigenvectors generated from a square plate on a 10×10 grid at $\kappa = 10$, in comparison to the corresponding on-diagonal value of ϵ . b) Heat map of $\log(|\text{Im}[\epsilon]|/\text{Im}[\epsilon]_{\max})$ corresponding to the thrust-producing modes, showing the relative magnitudes of the entries of the ϵ matrix.

III. THE VORTEX LATTICE MODEL

A. Methodology

The inviscid vortex lattice model (VLM) used in this work is based on that outlined by Katz and Plotkin (2001)⁴⁷, assuming small-amplitude motion and with modifications to enable frequency-domain modelling. Both 2D and 3D VLMs have been used extensively for first-order estimates of steady and unsteady airfoil loading, in a variety of applications such as wind and tidal energy^{48,49}, boat propellers⁵⁰, and aircraft wing modelling⁵¹. More recently, they have seen extensive use in the study of oscillating airfoils, propulsive kinematics and fluid-structure interaction^{39,52–54}. VLM in the format used in this paper gives results identical to classical inviscid airfoil theory such as the Theodorsen and Sears functions, for both steady and unsteady flow^{50,55}, and also performs well compared to high-order CFD simulations as long as separated flow effects are not dominant^{49,51}. The model presented below has been validated against both inviscid low-order and viscous high-order steady and unsteady simulations^{49,55}. Small-amplitude harmonic motion is assumed throughout.

As illustrated in Figure 2, the geometry is divided into panels (shown in grey) with associated vortex rings each made up of four vortex lines (shown in blue), and collocation points (marked in red). The surface coincides with the (x, y) -plane, and body thickness is not included in the model. The Kutta condition is implicitly enforced through the placement of the collocation point at 3/4th of each panel length, and the spanwise vortex lines at 1/4th panel length (see Katz and Plotkin⁴⁷). The wake vortices are formed as bound vorticity from the trailing edge panel is shed into the wake, moving along the horizontal coordinate at the steady relative freestream velocity U . Additional deformation of the wake through self-interaction (“vortex rollup”) is not included – this is not expected to significantly impact the results for small-amplitude perturbations, which are assumed through-

out this work. Because this paper uses a frequency-domain formulation, the relative freestream velocity U (representing the swimming speed) and the beat frequency ω (radians per second) are input variables.

The Biot-Savart law is used to find the velocity induced by each lattice vortex ring on each collocation point, such that the induced surface-normal velocity w on the m 'th collocation point by the n 'th vortex ring is given by

$$w_{mn} = \Gamma_n K_{mn} \quad (27)$$

where K is a kernel function based on the Biot-Savart law, determined by the geometry. If the n 'th vortex ring is made up of four vortex lines (see Figure 2) with the four corner locations connecting each vortex line having coordinates $\mathbf{p}_{n1} = [x_{n1}, y_{n1}, z_{n1}]$, $\mathbf{p}_{n2} = [x_{n2}, y_{n2}, z_{n2}]$ etc., and the m 'th collocation point has coordinates $\mathbf{c}_m = [x_m, y_m, z_m]$, then the kernel function is:

$$K_{mn} = \sum_{k=1}^4 \left[\frac{\mathbf{r}_{nk} \times \mathbf{r}_{n(k+1)}}{4\pi |\mathbf{r}_{nk} \times \mathbf{r}_{n(k+1)}|^2} \left(\frac{\mathbf{r}_0 \cdot \mathbf{r}_{nk}}{|\mathbf{r}_{nk}|} - \frac{\mathbf{r}_0 \cdot \mathbf{r}_{n(k+1)}}{|\mathbf{r}_{n(k+1)}|} \right) \right] \cdot \mathbf{n}_m \quad (28)$$

where $\mathbf{r}_0 = (\mathbf{p}_{n(k+1)} - \mathbf{p}_{nk})$, $\mathbf{r}_{nk} = (\mathbf{c}_m - \mathbf{p}_{nk})$ and $\mathbf{r}_{n(k+1)} = (\mathbf{c}_m - \mathbf{p}_{n(k+1)})$. The vector \mathbf{n}_m is the unit surface normal vector of the vortex panel at the m 'th collocation point. The relation between bound vorticity and wake vorticity is established by noting that the circulation of a wake panel at time t is the same as that of the trailing edge panel at time $t - k\Delta t$, where k is the number of time steps since the wake panel was shed from the trailing edge, such that for a harmonic system

$$\Gamma_k = \Gamma_{TE} e^{-(j\omega\Delta t)k} \quad (29)$$

where Γ_{TE} is the bound circulation at the upstream trailing edge panel. The time step Δt is an input variable in the present model, effectively determining the wake lattice resolution. Note that Equation 29 is dependent on ω , and thus on

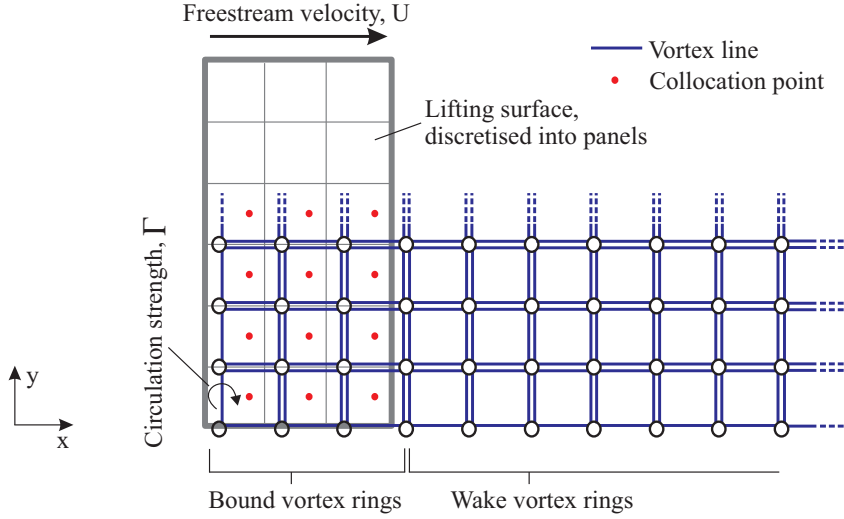


FIG. 2. Illustration of the vortex lattice model as applied to a rectangular wing.

the reduced frequency κ (Equation 2). As a result, the influence matrix in Equation 32 below – and its eigenmodes – will be κ -dependent.

The body motion is given by \mathbf{h} which indicates the surface distribution of displacement along the z -coordinate. The local velocity u is obtained from the heaving velocity $\partial h / \partial t = j\omega h$ and the surface-normal component of the freestream velocity. For small-amplitude motion, the relative surface-normal velocity due to the local pitch angle θ can be expressed as

$$U \sin(\theta(x, y, t)) \approx U \tan(\theta(x, y, t)) = -U \frac{\partial h(x, y, t)}{\partial x} \quad (30)$$

In matrix notation, this gives the surface-normal velocity from body movement as:

$$\mathbf{u} = (j\omega \mathbf{I} - U \mathbf{D}) \mathbf{h} = \mathbf{B} \mathbf{h} \quad (31)$$

where the matrix \mathbf{D} represents a numerical differentiation scheme for the vector \mathbf{h} . The eigenmode analysis was found to be sensitive to the choice of \mathbf{D} . Using forward or backward difference schemes produced significant scheme-dependent errors in the resulting eigenvector shapes, while a central difference scheme rectified the errors. All results presented below were obtained using a 6th order central difference scheme, with forward and backward schemes at the boundaries.

Finally, noting that $\mathbf{\Gamma} = \hat{\mathbf{\Gamma}} e^{j\omega t}$ and $\mathbf{h} = \hat{\mathbf{h}} e^{j\omega t}$, and that the exponentials will therefore cancel out, we relate the amplitude distributions of circulation to the body displacement through the following governing equation:

$$\mathbf{A} \hat{\mathbf{\Gamma}} = \mathbf{B} \hat{\mathbf{h}} \quad (32)$$

The matrix \mathbf{A} represents the transform of bound circulation to induced surface-normal velocity, and consists of combinations of Equations 28 and 29 for each lattice panel. Conventionally, the matrix \mathbf{A} would be inverted to find the vector of

unknown vortex circulation $\hat{\mathbf{\Gamma}}$, given a displacement $\hat{\mathbf{h}}$. However, in this study the eigenmodes obtained from the general eigenmode problem are found instead, and analyzed according to the method outlined in Section II. Having obtained the circulation vector $\hat{\mathbf{\Gamma}}$, in this case from Equation 5, the circulatory force is found from the vector form of the Kutta-Joukowski theorem (see Equation A1), and the added mass from Equation 12.

Lattice resolution studies were performed to remove mesh dependency. The convergence criteria used were applied to the main modes of interest (shown in the results sections below). They two criteria used were thrust coefficients not changing more than 5% when the mesh resolution was doubled, and that the eigenvector shapes did not visibly change. The most important parameters for convergence were found to be the chordwise lattice resolution, the streamwise wake resolution and the downstream extent of the wake. The chordwise resolution was consistently set to be as high as possible while maintaining achievable computational times (see Table I for the lattice resolutions used). The wake lattice resolution was set by specifying the implicit time step Δt . Two criteria on Δt were found necessary for accurate results. First, for N_c chordwise lattice panels:

$$\Delta t < \frac{c}{N_c U} \quad (33)$$

Second, it was necessary to ensure a minimum number of implicit time steps per harmonic period. In this study, this minimum limit was set to 300 time steps, such that:

$$\Delta t < \frac{2\pi}{300 \omega} \quad (34)$$

The streamwise extent of the wake was set to be 40 times the maximum chord or span length of the body geometry, whichever was the greater distance.

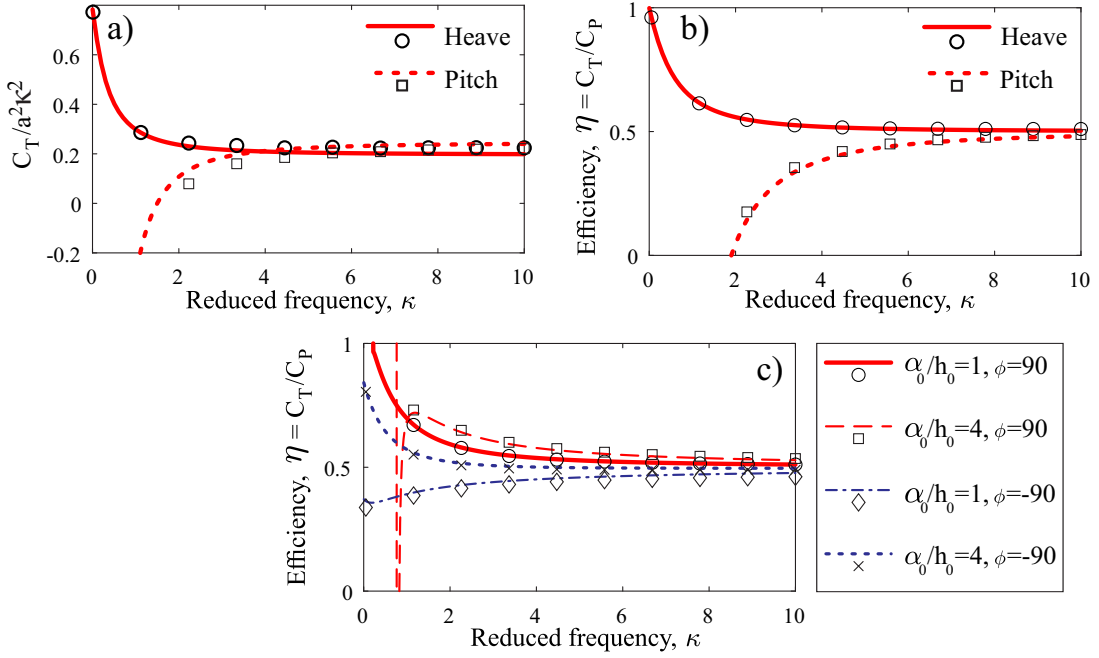


FIG. 3. 2D validation cases. Solid and dashed lines represent the analytical solution obtained by Garrick (1936)⁵⁶, while markers indicate the VLM solution. a) Normalised thrust coefficient of pure heave and pitch (for heave the amplitude a is in meters, while for pitch a is in radians), b) hydrodynamic efficiency of pure heave and pitch, c) hydrodynamic efficiency of combined heave and pitch, for heave amplitude h_0 and pitch amplitude α_0 .

B. Analysis of propulsive properties

The vortex lattice model outlined above was implemented in Matlab. The eigenmode decomposition is carried out as described in Section II, using the relevant Matlab functions to obtain the eigenvalues and eigenvectors of \mathbf{A} and \mathbf{B} . The thrust generated by each eigenmode is found by sequentially setting $\mathbf{h} = \mathbf{v}_R$ for each individual eigenvector and obtaining the corresponding circulation Γ . The results are expressed in terms of the cycle-averaged thrust coefficient, defined as:

$$C_T = \frac{\bar{T}}{\frac{1}{2}\rho U^2 S} \quad (35)$$

In order to evaluate the Froude efficiency (Equation 1) the cycle-average power coefficient is also evaluated, defined as:

$$C_P = \frac{\bar{P}}{\frac{1}{2}\rho U^3 S} \quad (36)$$

The power is defined as the inner product of the body force with the transverse body velocity (see Equations 18 and A5). The efficiency is then given as:

$$\eta = \frac{C_T}{C_P} \quad (37)$$

In the results below the thrust coefficient is normalised by a^2 to remove the dependence on beat amplitude from the re-

sults, which is trivial for small-amplitude inviscid modelling. It is further normalised by κ^2 .

Since the present study uses an inviscid vortex lattice model, assuming small-amplitude motion, the Strouhal number (Equation 3) is of value only as it relates to the reduced frequency, since the cycle-average thrust scales with amplitude as $T \propto a^2$. As such, the effects of Strouhal number are not considered below, but only the effects of reduced frequency κ (Equation 2).

C. Validation

Previous validation of the VLM code focused on prediction of lift as a result of unsteady gust forcing^{49,55}. The code used in the present study is also validated against the work of Garrick (1936)⁵⁶, who extended Theodorsen's analysis to include thrust prediction for heaving and pitching plates. The set of assumptions underlying Garrick's model – inviscid small-amplitude flow with a planar wake, also used for the VLM in Section III – have been shown to be limited in its ability to predict thrust and propulsive efficiency by several past and recent studies^{4,28,57}, suggesting that these assumptions may not accurately represent the flow physics of oscillating airfoils. While acknowledging these limitations, the assumptions of inviscid small-amplitude flow may still have value in providing a theoretical upper limit on swimming efficiency, which justifies its use in this paper for demonstrating the eigenmode analysis presented in Section II. As mentioned above, the eigenmode analysis can also be applied to more advanced hydrodynamic

Shape	Resolution
Square	$[120 \times 40]$
Rectangle	$[200 \times 31]$
Rectangular wing	$[80 \times 30]$
Ellipse	$[80 \times 60]$
Tapered wing	$[80 \times 80]$

TABLE I. Lattice resolutions for the geometries shown in Figure 4, shown as [number of chordwise panels \times number of spanwise panels].

models including more realistic flow physics, which is a topic for further work.

The cycle-average thrust coefficient given by VLM is shown in Figure 3a for a 2D plate in pure heave and when pitching about the quarter-chord. The corresponding propulsive efficiencies are given in Figure 3b. The propulsive efficiencies resulting from a combination of pitch at amplitude α_0 and heave at amplitude h_0 , for various relative amplitudes and phases, are shown in Figure 3c. The 2D results were obtained from the 3D VLM by evaluating the result at mid-span of a large aspect ratio wing ($AR = 100$ with 100 chordwise panels and 5 spanwise panels). The results show good agreement with Garrick’s analytical function.

D. Body planforms

Figure 4 illustrates the geometries analyzed in this paper. Figure 4a shows the square plate used to demonstrate the salient properties of the eigenmodes. The rectangle geometries in Figures 4b and 4c are used to study the effects of aspect ratio (0.25 and 2.85 respectively). The two remaining planforms were chosen to have qualitatively similar features to swimmers found in nature; the ellipse in Figure 4d represents the simplified outline of a marine flatworm, while Figure 4e shows a tapered wing inspired by the shape of a manta ray. The tips of the tapered wing are cut off (an approach also used successfully by Ayancik et al. (2020)³⁹ to study tail fin propulsion), since the VLM cannot model the chord length tapering to zero.

IV. HYDRODYNAMIC EIGENMODE ANALYSIS OF A SQUARE PLATE

A. Eigenvalues and eigenvector shapes

Figure 5 shows the eigenvalues of the governing equation (Eq. 32) for $\kappa = 1.0$ for the square plate geometry. A selection of associated right eigenvectors are shown in Figure 6. The eigenvalues are normalised by the chordwise number of vortex lattice panels n .

The eigenvalues visible in Figure 5 can be separated into two groups: the “core” eigenvalues (expanded view), and the “outer” eigenvalues which are two orders of magnitude larger than those in the core. The former are of primary interest in

this study, as the outer eigenvalues are highly grid-dependent and as such are likely to be an artefact of the discretized domain. By contrast, the core modes do not change significantly with increasing grid resolution. As such, in the rest of the paper only the core modes will be considered for each geometry.

The core eigenvalues in Figure 5 show clear groupings into radial segments, or “branches”. Four such segments have been chosen for illustration and are marked 1-4 in Figure 5, with successive eigenvalues within a segment marked *.a*, *.b*, *.c*, etc. starting from the innermost eigenvalue. The corresponding right eigenvectors for these modes are shown in Figure 6, illustrated as contour plots of surface displacement. Figure 6 shows that moving outward along the branch (from *.a* \rightarrow *.b* \rightarrow *.c*, etc.) corresponds to a stepwise increase in spanwise wavenumber in the eigenvectors, in increments of half-wavenumbers. This trend is consistent for all the eigenvectors identified from all the geometries used in this study. Moving further radially outwards, eventually the wavelengths become too short to be properly resolved, and the modes resemble noise. The mode shapes from the various branches 1, 2, 3 and 4 in Figure 6 are qualitatively similar, with subtle differences in amplitude distributions and in phase. 3D visualisation of the swimming kinematics resulting from the eigenvectors in Figure 6 can be seen in Figure 7 (multimedia view).

The modes observed in Figures 5 and 6 undergo substantial change with increasing reduced frequency. Figure 8 shows the eigenvalues for $\kappa = 1.0, 2.0, 3.0$ and 4.0 . The eigenvalue branches shift positions in the complex plane; of particular interest is the movement of branch 3 from positive to negative complex semi-plane. As κ is increased further, successive branches continue to move from positive to negative complex components. It will be shown below that when the imaginary component of an eigenvalue moves from positive to negative, the corresponding eigenvector starts to produce thrust. Note that the positional shift of branch 2 in Figure 8 is distinct from the others. It will be shown below that the associated eigenvectors have unique properties compared to the other modes.

Looking at the eigenvectors, at low κ (as in Figure 6) there is limited chordwise variation in the motion amplitude, such that the modes exhibit relatively uniform “flapping” motion (see Figure 7 – multimedia view). Figure 9 shows how two vectors from Figure 6 change shape as κ increases. Figure 9a shows Mode 2.a for increasing κ , and Figure 9b shows the 3D visualisation of the kinematics of the same mode (multimedia view). The chordwise wavelength of the mode can be seen to gradually decrease with increasing κ . The same behaviour is seen for Mode 3.a in Figure 9c, with Figure 9d showing the 3D visualisation of the kinematics (multimedia view). Using the terminology of Smits (2019)¹⁷, the eigenvectors produce “oscillatory” kinematics at low reduced frequencies, and as the frequency increases the motion pattern gradually shifts to “undulatory”. This is a consistent behaviour for all modes identified in this study.

A notable difference between Mode 2.a and Mode 3.a in Figure 9 is in the location of peak motion amplitude. As κ increases, the peak amplitude of Mode 2.a shifts to the trailing edge. Mode 3.a, by contrast, retains a uniform amplitude dis-

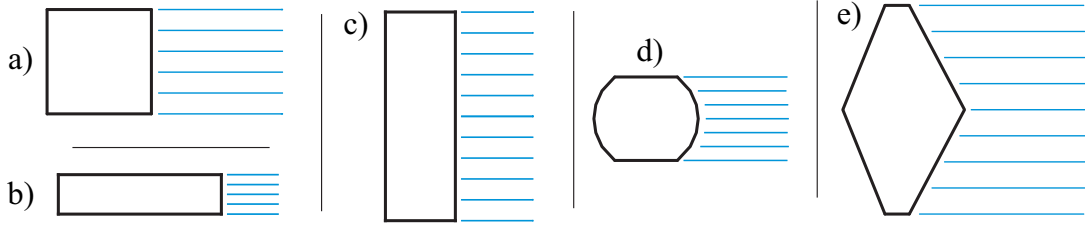


FIG. 4. The geometries analyzed (black), with corresponding streamwise wake vortex lines (blue). a) Square plate, b) elongated rectangular plate (aspect ratio 0.25), c) rectangular wing (aspect ratio 2.85), d) elliptical geometry, and e) tapered wing. See Table I for details of the lattice resolution.

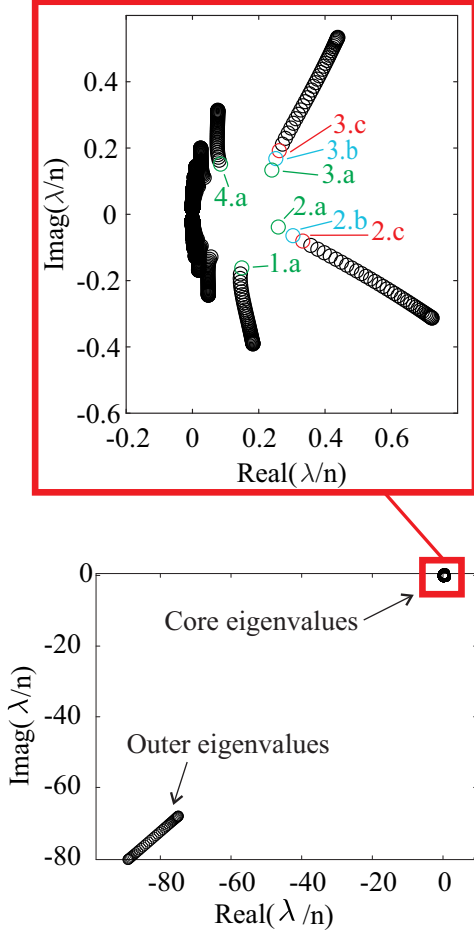


FIG. 5. The square plate eigenvalues for $\kappa = 1$. The eigenvalue branches of interest are marked 1-4, with the three innermost eigenvalues of each branch marked .a, .b and .c.

tribution along the chord at all frequencies. The kinematics of Mode 2.a is qualitatively similar to swimming motions seen in many marine animals, in which the amplitude of motion tends to gradually increase along the body and peak at the trailing edge. Only the eigenvectors associated with eigenvalue branch 2 exhibited this behaviour, and it will be shown that the other geometries evaluated below exhibit a similar trend in a small selection of eigenvectors.

B. Propulsive properties: thrust and efficiency

Figure 10 shows the thrust coefficients and Froude efficiencies resulting from the eigenvector kinematics obtained from the square plate, for $\kappa = 5.0$. Prior to analysis a filtering process was applied to identify and discard modes with spanwise and chordwise wavenumbers too high to be physically feasible. A limit on the second derivative of surface displacement was set, in order to limit the maximum allowable body curvature. At the top of Figure 10 two eigenvectors are included as examples of modes which did or did not pass the filtering process. It can be seen in Figure 10a that just over half of the modes identified produce positive thrust at this frequency. The propulsive efficiencies in Figure 10b are above 70% for all modes, and exceeds 95% for a majority.

Having identified a subset of potentially viable modes through the filtering process, we can now study mode properties with changing κ . All eigenvectors in Figure 6 have physically realistic spanwise and chordwise wavenumbers, and so the propulsive properties of Modes 1-4.a are shown in Figure 11 to illustrate the effect of κ (legend notation as in Figures 5 and 6).

Looking at the thrust (Figure 11a), at low κ there are substantial differences between the modes, while all modes approach a similar trend at higher κ . The eigenvalues of Mode 1.a and Mode 2.a have negative complex components throughout the tested frequency range (see Figure 8), and they can be seen to always produce positive thrust. Mode 2.a reaches and maintains a level value of about 0.01 as κ increases, suggesting that the thrust is proportional to κ^2 . Modes 3.a and 4.a start producing thrust at $\kappa = 3.0$ and $\kappa = 7.0$ respectively; these are the frequencies at which their corresponding eigenvalues shifts from positive to the negative complex space.

In the Froude efficiency (Figure 11b) the modes fall in two clear categories, where Modes 1.a, 3.a and 4.a all have efficiencies of 95% or higher while Mode 2.a varies at lower κ and then approaches a level value in the range 75-80%. While the efficiency of Mode 2.a is lower than the others, it is higher than that of heaving and pitching motion at similar frequencies (see Figure 3). The benefit of Mode 2.a is that its motion amplitude increases gradually from leading to trailing edge, as can be seen in Figure 9b, while the other modes have consistently large leading-edge amplitudes. As such, Mode 2.a has an advantage in a viscous flow where leading edge stall must be avoided.

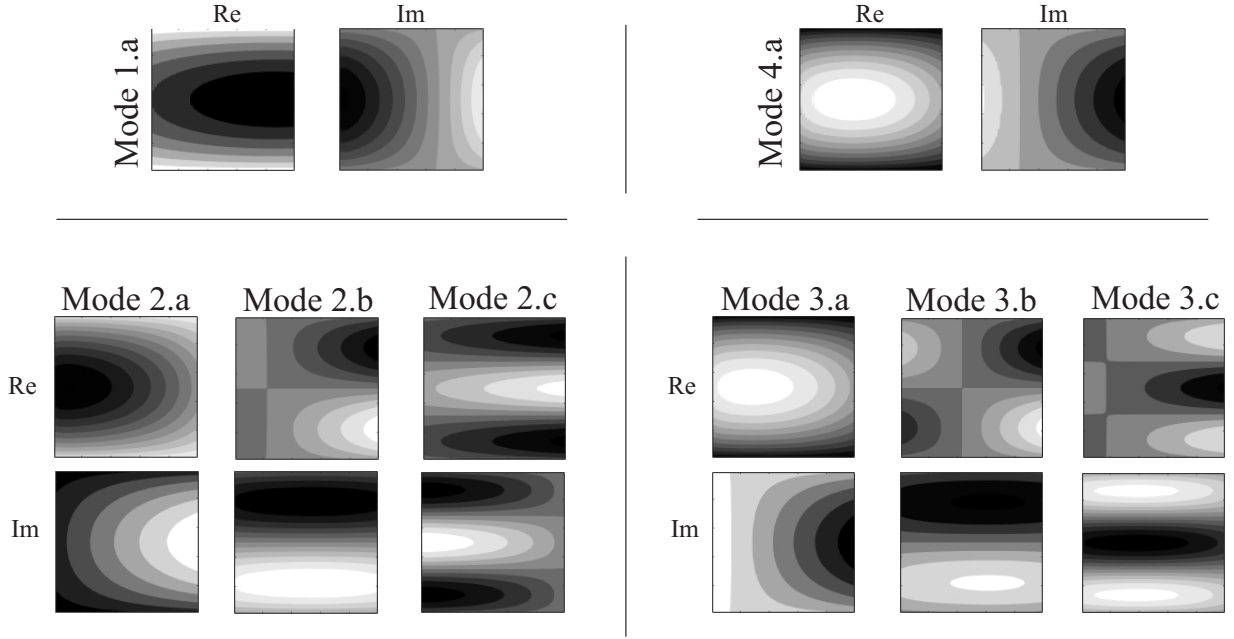


FIG. 6. Contour plots illustrating the real and imaginary parts of a selection of eigenvectors corresponding to the eigenvalues in Figure 5, for $\kappa = 1$.

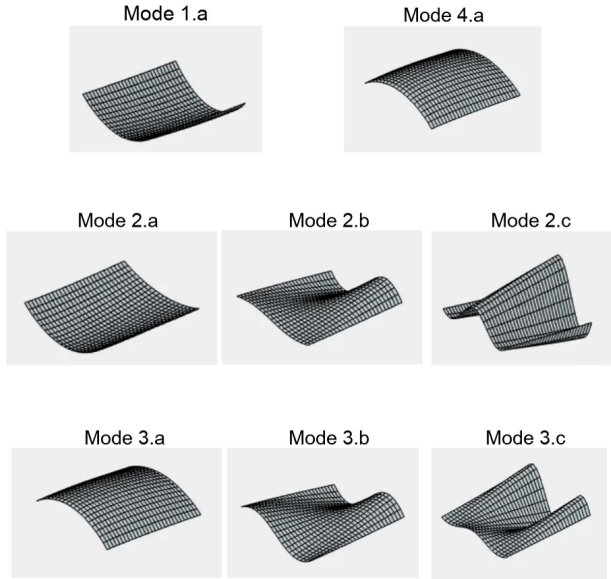


FIG. 7. 3D illustrations of the swimming kinematics corresponding to the eigenvectors in Figure 6 (multimedia view).

C. Summary of notable features

A number of features found in the eigenmodes of the square plate recur in the other geometries tested. They are summarized here.

The eigenvalues are grouped together in separate distinct

“branches”, the positions of which shift in complex space as the reduced frequency increases. The modes of “branch 2” have distinct properties compared to the other modes.

Moving outwards along a branch of eigenvalues corresponds to a stepwise increase in spanwise wavenumber of the corresponding eigenvector. Increasing κ results in an increase in the chordwise wavenumber of all eigenvectors.

The eigenvectors associate with branch 2 uniquely have the feature of increasing motion amplitude from the leading to the trailing edge, which is a feature often seen in marine animal swimming. All other modes have amplitudes more uniformly distributed in the chordwise direction.

The modes start producing thrust at a certain “cut-in frequency” κ_c , which corresponds to the complex component of the corresponding eigenvalue going from positive to negative. Above the cut-in frequency the modes generally have propulsive efficiencies of over 90%, the exception being the kinematics obtained from modes in branch 2, which give efficiencies of over 70%. The high efficiencies persist for increasing κ , in contrast to pure heaving or pitching motion for which the propulsive efficiency decreases at high κ (see Figure 3). While the efficiencies of the various modes are similar (apart from modes in branch 2) the differences in their thrust coefficients are more significant.

V. HYDRODYNAMIC EIGENMODE ANALYSIS OF RECTANGULAR PLATES

A. Analysis of elongated plate planform

Figure 12 shows summary results of the hydrodynamic eigenmode analysis for the elongated plate in Figure 4b. The

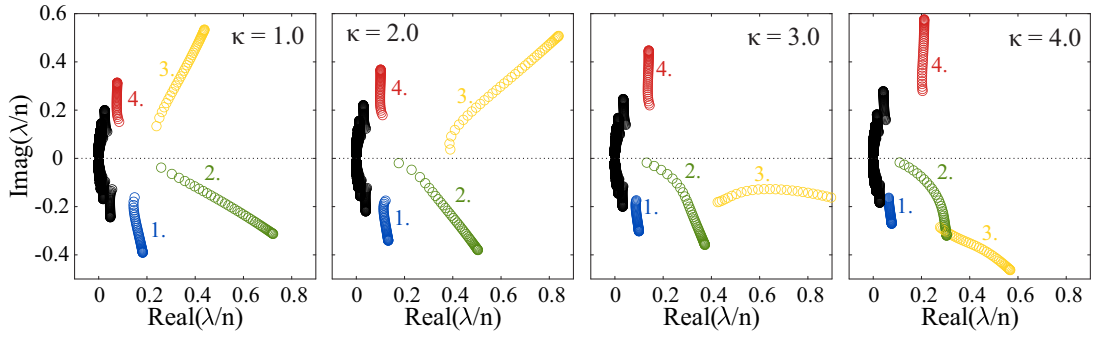


FIG. 8. The square plate eigenvalues for different values of reduced frequency κ . The eigenvalue branches of interest are marked 1-4.

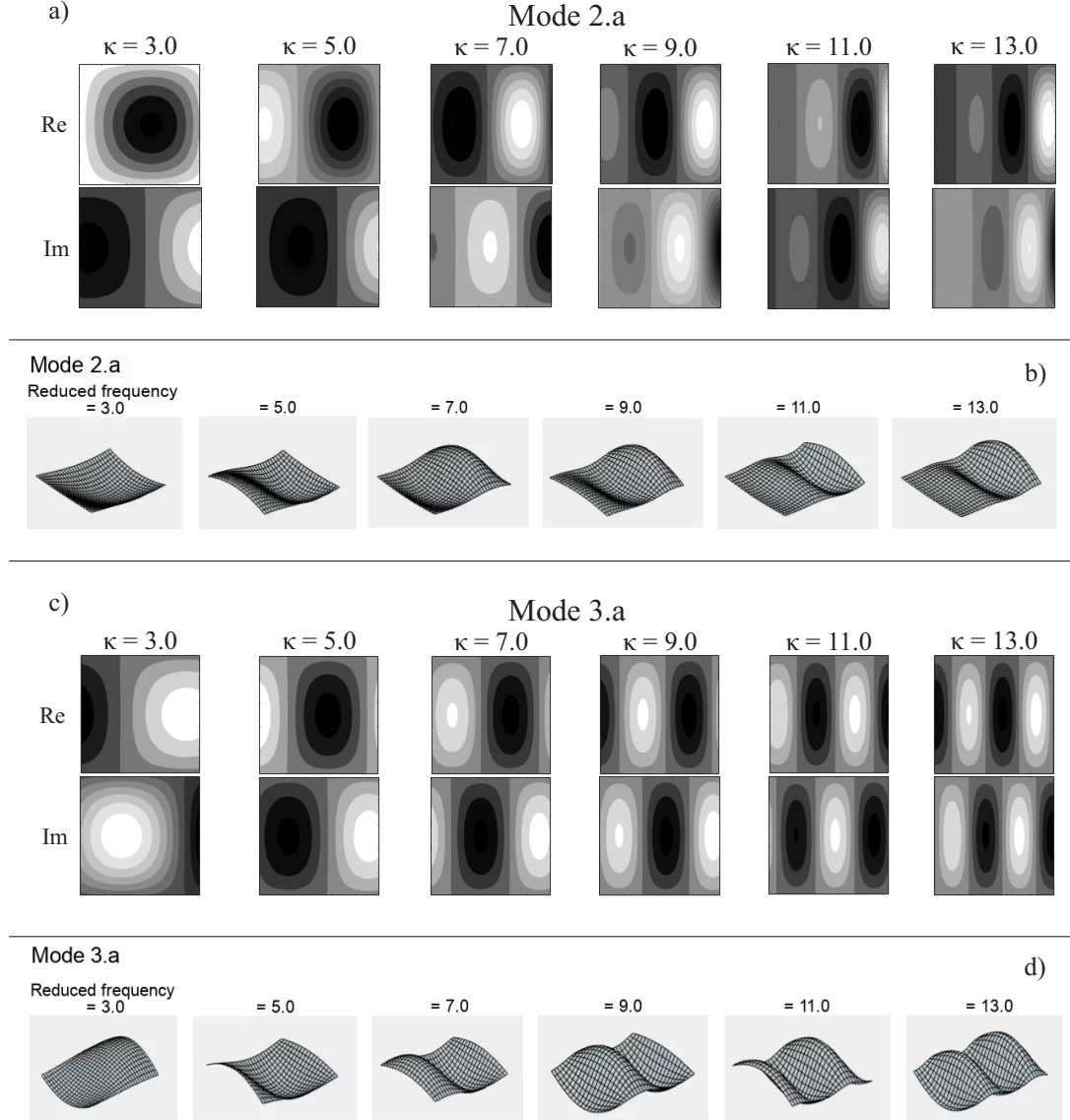


FIG. 9. Illustration of the changing shapes of Mode 2.a and Mode 3.a (see Figures 5 and 6) with increasing reduced frequency κ . a) Real and imaginary contours of Mode 2.a, b) 3D illustrations of the swimming kinematics corresponding to Mode 2.a, obtained by multiplying the real component by $\exp(j\omega t)$ for a range of t (multimedia view), c) Real and imaginary contours of Mode 3.a, d) 3D illustrations of the swimming kinematics corresponding to Mode 3.a, obtained by multiplying the real component by $\exp(j\omega t)$ for a range of t (multimedia view).

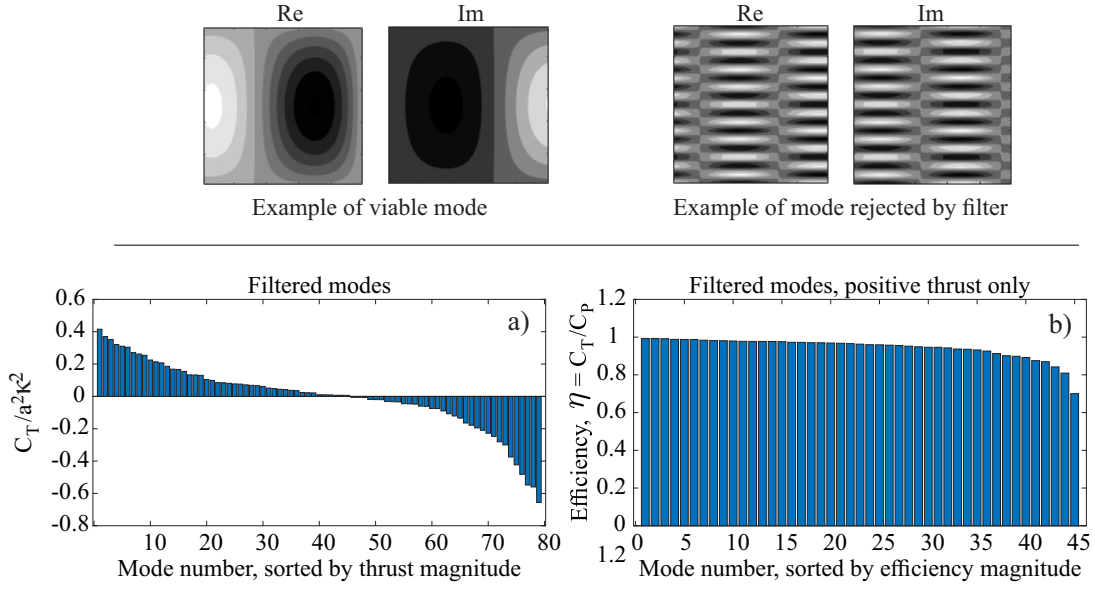


FIG. 10. Top: Illustration of two example eigenvectors for the square plate eigenmodes at $\kappa = 5.0$, subjected to mode filtering based on surface curvature. a) Normalised thrust coefficient and b) efficiency of the filtered modes for $\kappa = 5.0$. Note that only efficiencies from positive-thrust cases are included.

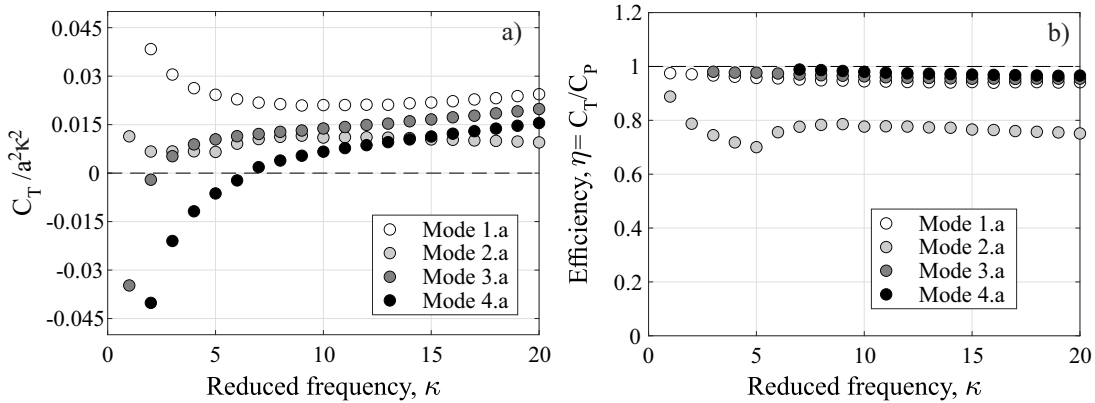


FIG. 11. a) Normalised thrust and b) Froude efficiency (only efficiencies from positive-thrust cases are included) for increasing reduced frequency κ for a selection of eigenvectors from the square plate. Legend notation corresponds to that of Figure 5.

eigenvalues (Figure 12a), shown for $\kappa = 1.0$, are structured in radial branches similar to those of the square plate in Figure 5. Three associated eigenvectors (Modes 2.a, 3.a and 5.a) are shown in Figure 12b, all representing the innermost eigenvalue in their respective branch. The eigenvectors are evaluated at $\kappa = 1.0$, 5.0 and 9.0. Note that these eigenvectors do not necessarily correspond to the peak-performing modes, but are chosen to illustrate general trends in the eigenvector shapes.

As for the square plate in Figure 9, the chordwise wavenumbers of the eigenvectors in Figure 12b increase with κ . There are subtle differences between the eigenvectors; the chordwise wavenumber of Mode 5.a is about 25% higher than Mode 3.a for $\kappa = 5.0$ and 9.0. As κ increases, the maximum motion amplitude of Mode 2.a shifts to the trailing edge (as was the case for Mode 2.a in Figure 9).

Figure 12c shows the thrust produced by Modes 1-

5.a (corresponding to the innermost eigenvalues of each branch marked in Figure 12a) for increasing κ . Again the modes whose eigenvalues have negative complex components throughout this frequency range (Modes 1.a and 2.a) always produce positive thrust, while Modes 3.a, 4.a and 5.a produce thrust only above a certain cut-in frequency κ_c which coincides with their eigenvalues moving from positive to negative complex space. Interestingly, the cut-in frequencies for the modes in Figure 12c are the same as for the corresponding square plate modes in Figure 11a, e.g. $\kappa_c \approx 7.0$ for Mode 4.a in both cases. While the trends of the elongated plate are similar to those of the square plate, the magnitude of the normalised thrust coefficient in Figure 12c settles on a value approximately half that of the square plate in Figure 11a at comparable κ . There is more significant variation in the thrust coefficient of the different modes in Figure 12c compared to

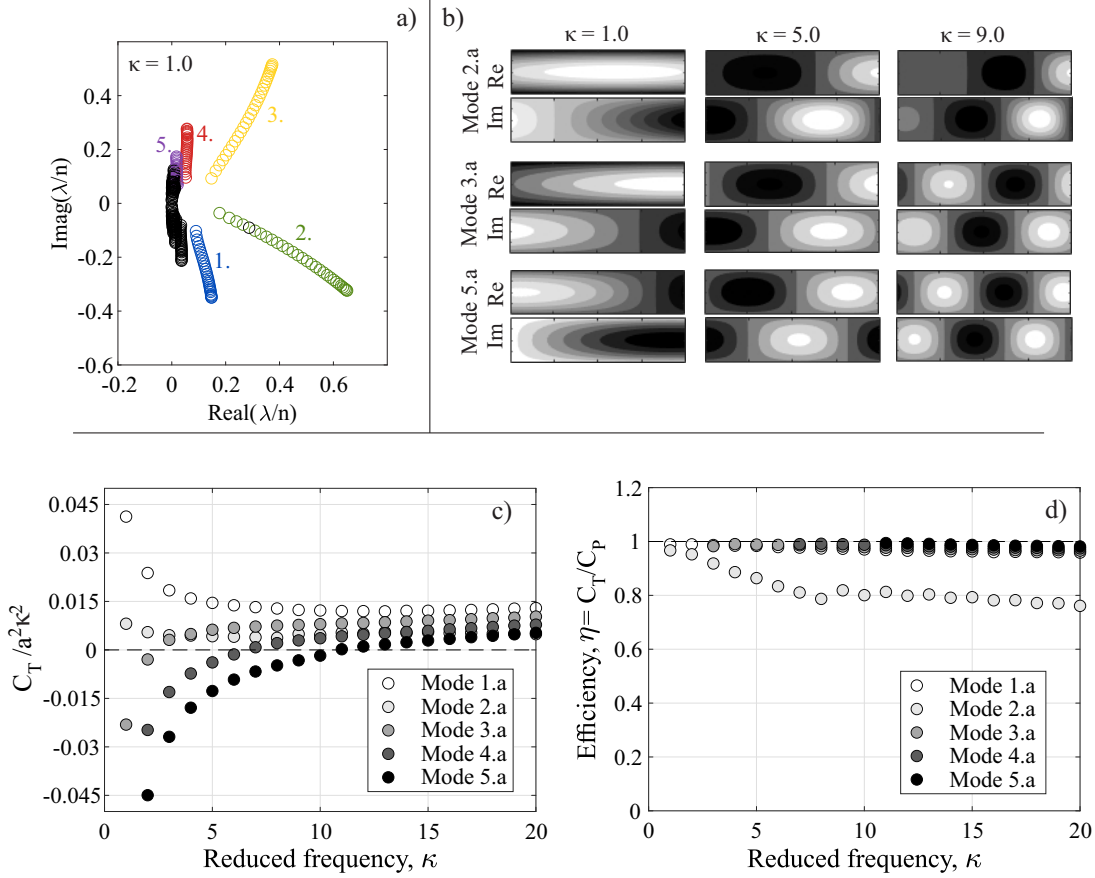


FIG. 12. a) Eigenvalues, b) eigenvectors, c) thrust and d) efficiency of a selection of eigenvectors from the elongated plate geometry. The eigenvalue branches of interest are marked 1-5 in the eigenvalue plot.

the variation in efficiency in Figure 12d, apart from Mode 2.a.

Looking at the Froude efficiency in Figure 12d, the trends are again similar to those of the square plate in Figure 11b. Modes 1.a, 3.a, 4.a and 5.a all have efficiencies close to 100%, while Mode 2.a has efficiency near 100% at $\kappa = 1.0$ and then decreases to reach a level value of about 80%. This again demonstrates that the eigenmodes can reach efficiencies significantly higher than pure pitching or heaving motion (see Figure 3).

B. Analysis of rectangular wing planform

Figure 13 shows summary results from hydrodynamic eigenmode analysis of the rectangular wing geometry in Figure 4c. Figure 13a shows the eigenvalues at $\kappa = 1.0$, while Figure 13b shows eigenvectors corresponding to the three innermost eigenvalues on branch 2 and 3, marked Mode 2.a-c and Mode 3.a-c, for different frequencies. Again, the modes shown are not necessarily the peak-performing modes, but are chosen to illustrate general properties of the eigenvectors.

As in Figure 6, the eigenvectors exhibit a stepwise increase in spanwise wavenumber, with a half-wavenumber added for each outward step in the branch of eigenvalues ($.a \rightarrow .b \rightarrow .c$). The spanwise wavenumber is unchanged with κ , while the

chordwise wavenumber increases with increasing κ as before. The maximum movement amplitudes of Modes 2.a-c shifts to the trailing edge with increasing κ , while Modes 3.a-c retain a uniform amplitude distribution.

Figures 13c and 13d respectively show the thrust and Froude efficiency of Modes 1.a and 4.a, while Figures 13e and 13f show that of Modes 2.a-c and 3.a-c. The thrust results (Figures 13c and 13e) show varying cut-in frequencies κ_c between the modes, and as before κ_c corresponds to a shift of the corresponding eigenvalue from positive to negative complex space. Modes originating from the same branch of eigenvalues appear to have close to identical propulsive properties according to Figures 13e-f, except for the low- κ response of Modes 2.a-c. Mode 3.a and 4.a again have the same cut-in frequencies as the corresponding modes from the square and elongated plates above (Figures 11 and 12), at $\kappa_c \approx 3.0$ and 7.0 respectively. The thrust magnitudes for the modes in Figures 13c and 13e are slightly larger than that of the square plate, with Modes 2.a-c settling at about $C_T/a^2\kappa^2 = 0.017$.

The Froude efficiencies in Figures 13d and 13f are consistently high, exceeding 70% everywhere except at $\kappa = 2.0$ and 3.0 for Mode 2.a, which is higher than can be achieved through pure pitching or heaving. As before, the modes associated with eigenvalue branch 2 have lower efficiencies than the other modes.

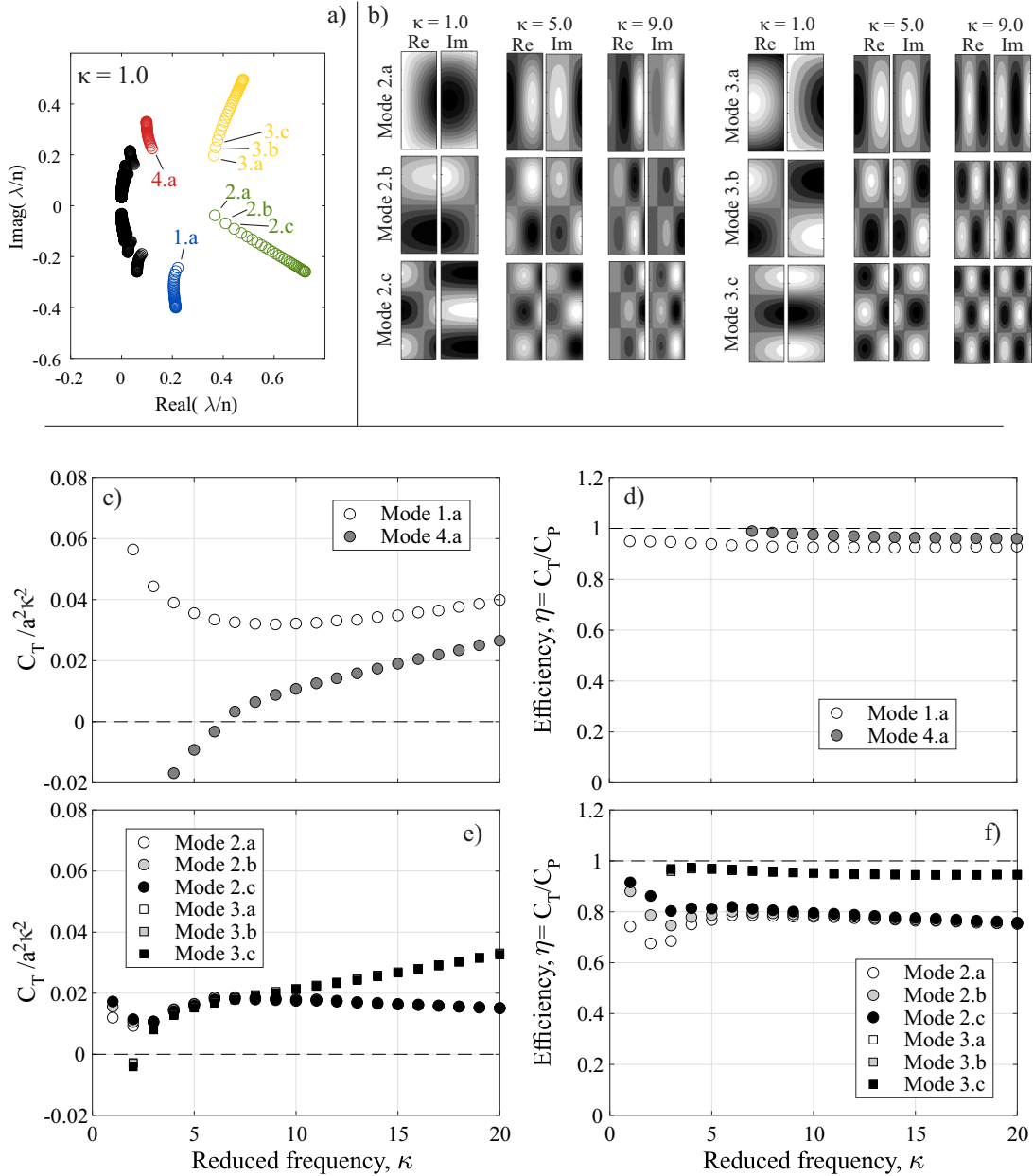


FIG. 13. a) Eigenvalues and b) eigenvectors of a selection of eigenvectors from the rectangular wing geometry. c) and e) shows normalised thrust, while d) and f) shows Froude efficiency. The eigenvalue branches of interest are marked 1-4 in the eigenvalue plot, with the three innermost eigenvalues in a branch marked *a*, *b* and *c*.

VI. HYDRODYNAMIC EIGENMODE ANALYSIS OF BIO-INSPIRED GEOMETRIES

A. Analysis of elliptical planform

Figure 14 shows eigenvalues for the elliptical plate (Figure 4d), evaluated at different frequencies. The structure of the eigenvalues is similar to that of the rectangular geometries above (e.g. in Figure 5), but additional features emerge with increasing κ . Each branch of eigenvalues divides into “sub-branches” as the eigenvalues move from positive to negative

complex space, as can be seen for the eigenvalues associated with branch 3 in Figure 14. The eigenvectors associated with these sub-branches were generally found to be “noisy” with high surface curvatures, and so were discarded in the mode filtering process described in Section IV.

Figure 14 also shows three eigenvectors each evaluated at different κ ; Modes 3.a, 4.a and 5.a, corresponding to the innermost eigenvalue in branches 3-5. The spanwise wavenumber changes with κ for all three modes, in contrast to the eigenvectors of the rectangular geometries above. Looking at Mode 3.a, the amplitude of motion becomes increasingly concentrated around the centreline as κ increases. The mo-

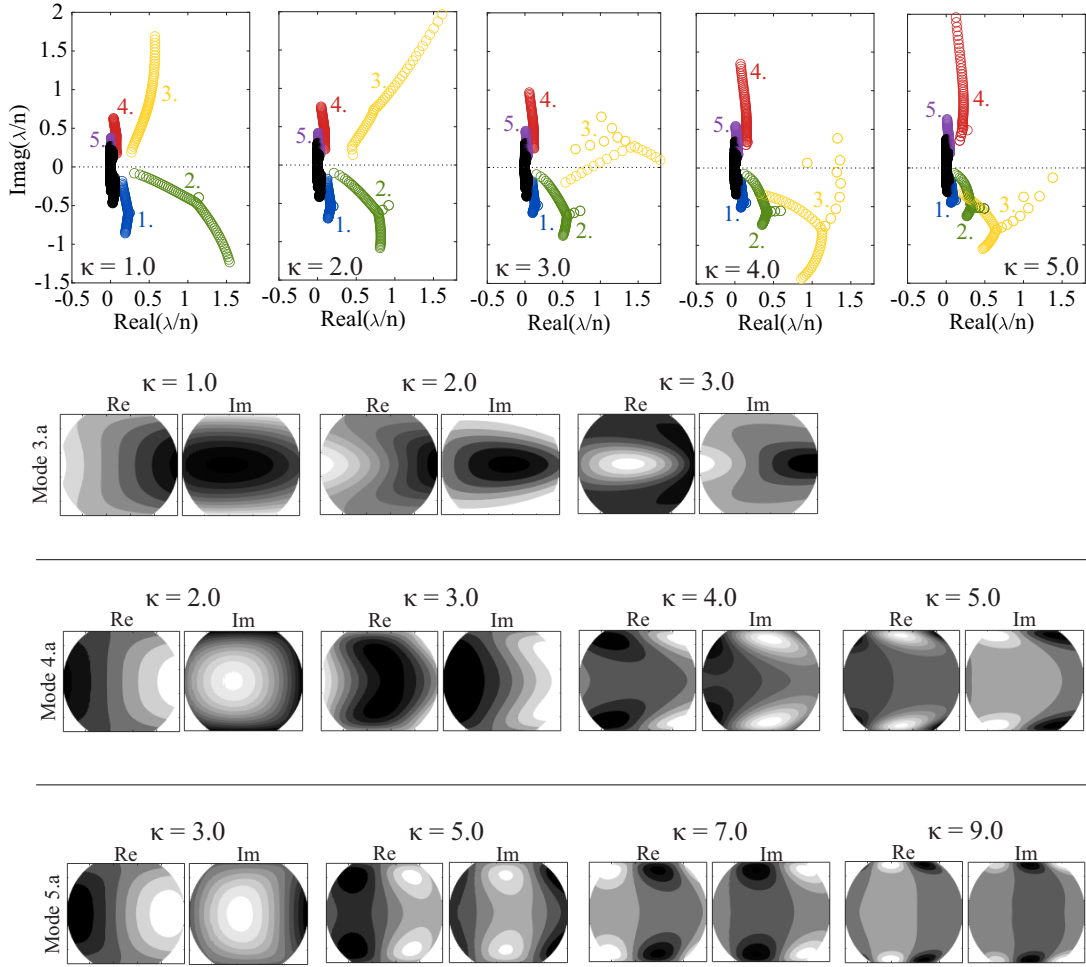


FIG. 14. Eigenvalues and right eigenvectors obtained from the elliptical geometry. The eigenvalue branches of interest are marked 1-5 in the eigenvalue plots.

tion amplitudes of Modes 4.a and 5.a on the other hand shift towards the spanwise edges as κ increases, such that eventually the centreline is stationary. The outcome is an effective increase in the spanwise wavenumber with increasing κ for all three modes. There is an increase in chordwise wavenumber with increasing κ as before, but the change is dominated by the spanwise wavenumber.

Figure 15 shows the thrust and propulsive efficiency of Modes 1.a-5.a, representing the innermost eigenvalue of each branch marked in Figure 14, against κ . The normalised thrust coefficient (Figure 15a) undergoes substantial change at low κ , and approaches a settled value as κ increases, indicating a κ^2 proportionality in the cycle-average thrust. The highest settled thrust value, approximately $C_T/a^2\kappa^2 = 0.02$ produced by Mode 1.a, is higher than that achieved by the square plate in Section IV. The eigenvalues of Modes 4.a and 5.a are in the positive complex plane at low κ , but in contrast to the rectangular geometries above they do not shift to the negative complex plane as κ increases. Consequently, they do not produce net positive thrust at any of the frequencies evaluated.

The Froude efficiency is given in Figure 15b. As for the rectangular geometries, the efficiencies are generally above

70%, with Modes 1.a and 3.a outperforming Mode 2.a. Once again, the eigenmodes consistently produce propulsive motion with efficiencies higher than that of pure heaving or pitching.

B. Analysis of tapered wing planform

Figure 16 shows the eigenvalues of the tapered wing geometry (Figure 4e) evaluated at $\kappa = 3.0$, and also a selection of eigenvectors for different frequencies. As with the elliptical geometry above, the eigenvalues are grouped in branches with new “sub-branches” emerging when moving from positive to negative complex space. The main region of interest in the eigenvalue plot in Figure 16 is expanded.

Looking at the eigenvectors in Figure 16, Mode 2.a-c (corresponding to the three innermost eigenvalues of branch 2) follow the same pattern as the square plate and rectangular wing above: there is a stepwise increase in wavenumber in increments of 0.5 when moving outwards in the eigenvalue branch ($.a \rightarrow .b \rightarrow .c$). As κ increases this pattern persists while the chordwise wavenumber increases. However, similar to the elliptical geometry, the amplitude of motion also

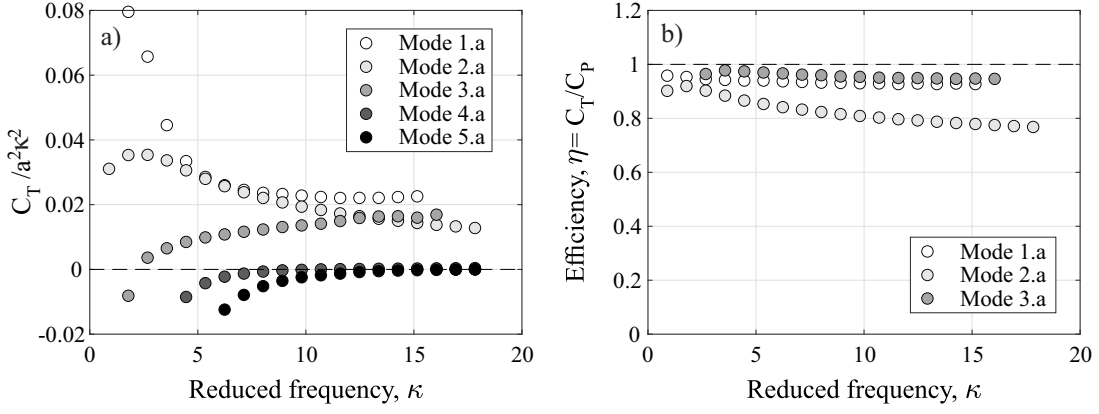


FIG. 15. Propulsive properties against reduced frequency κ for a selection of eigenvectors from the elliptical geometry. The legend notation corresponds to that of Figure 14. a) Normalised thrust, b) Froude efficiency (note that only efficiencies from positive-thrust cases are included).

becomes increasingly concentrated around the centreline.

Modes 1.a* and 2.a* are associated with the eigenvalue “sub-branches”, and do not correspond in nature to any other modes found in other geometries evaluated in this paper. As was the case for some modes from the elliptical geometry, the motion amplitudes of these modes become increasingly concentrated near the spanwise edges with increasing κ , while the centreline is stationary. The spanwise wavenumber of Mode 2.a* increases rapidly with increasing κ , such that the surface curvature quickly becomes non-physical and the mode is rejected by the filtering process. The spanwise wavenumber of Mode 1.a* undergoes less change, and the surface curvature remains physically viable. For both Modes 1.a* and 2.a* the change to the spanwise wavenumber exceeds that of the chordwise wavenumber as κ increases.

Figure 17 shows the propulsive properties of the modes included in Figure 16, with the thrust and Froude efficiency of modes from branch 1 shown in Figures 17a-b and those of modes in branch 2 in Figures 17c-d. Note that only motion frequencies up to $\kappa = 10.0$ were evaluated for this geometry, since higher frequencies resulted in large surface curvatures across virtually all modes, rendering these frequencies less physically meaningful.

Looking at the thrust in Figures 17a and 17c, the normalised thrust coefficient approaches a level value in the range $C_T/a^2\kappa^2 \approx 0.01 - 0.02$ with increasing κ (exceptions being Mode 1.a* and Mode 2.a*, which settle at lower values). Both the behaviour and the settling range of the normalised thrust coefficient are remarkably similar to those of the modes associated with the other geometries analyzed in this study. Looking at the Froude efficiency, the modes associated with branch 1 (Figure 17b) have higher efficiencies than those of branch 2 (Figure 17d) – 95% vs $\eta \approx 80\%$. Note that the properties of Mode 2.a* are shown only up to $\kappa = 4.0$, since beyond this frequency the spanwise wavenumber of this mode was too high to be physically meaningful. The same applies to Mode 1.a-c, which are only included up to $\kappa = 7.0$.

The results in this section and Section VI A show that while the eigenmodes of the different geometries in Figure 4 have many propulsive features in common, changing body plan-

form has the potential to produce new eigenmodes or mode behaviours. Examples of this include Mode 1.a* and Mode 2.a* for the tapered wing in Figure 16, and Mode 4.a and Mode 5.a from the elliptical geometry (Figure 14).

VII. DISCUSSION

In this paper we use well-established hydrodynamic modelling methods to numerically compute the eigenmodes of the unsteady potential flow problem for a thin-bodied swimmer of arbitrary three-dimensional planform, and we demonstrate that high-efficiency swimming kinematics can be generated from these eigenmodes.

The results in Sections IV-VI show that the eigenmodes can generate high-efficiency kinematics, and also that high hydrodynamic efficiency can be achieved for any body geometry as long as the appropriate swimming kinematics are used: the peak efficiency resulting from the eigenmodes was the same for all geometries tested ($> 95\%$ – note that this result is obtained from an inviscid model). This is similar to the conclusions drawn by Zurman-Nasution et al. (2021)⁵⁸, who found no significant variation in efficiency across tail fin sweep angle, and Ayancik et al. (2020)³⁹ who similarly found little variation in efficiency across a selection of tail fin shapes from marine animals. In both cases, as long as the kinematics of the fin motion was appropriate, high-efficiency swimming could be achieved for any fin geometry.

The results from Sections IV-V of this paper suggest that both low and high aspect ratio geometries can generate motion of high inviscid propulsive efficiency, as long as an appropriate mode is used and the frequency is above the cut-in frequency. This contrasts with traditional understanding which states that decreasing the aspect ratio reduces propulsive efficiency²⁰. However, Dong et al. (2006)⁶ showed through numerical simulations that the hydrodynamic efficiency of flapping wings with different aspect ratios approached the same value when κ was increased, although the wing with the highest aspect ratio still exhibited the highest overall efficiency and the lowest aspect ratio tested did not reach the

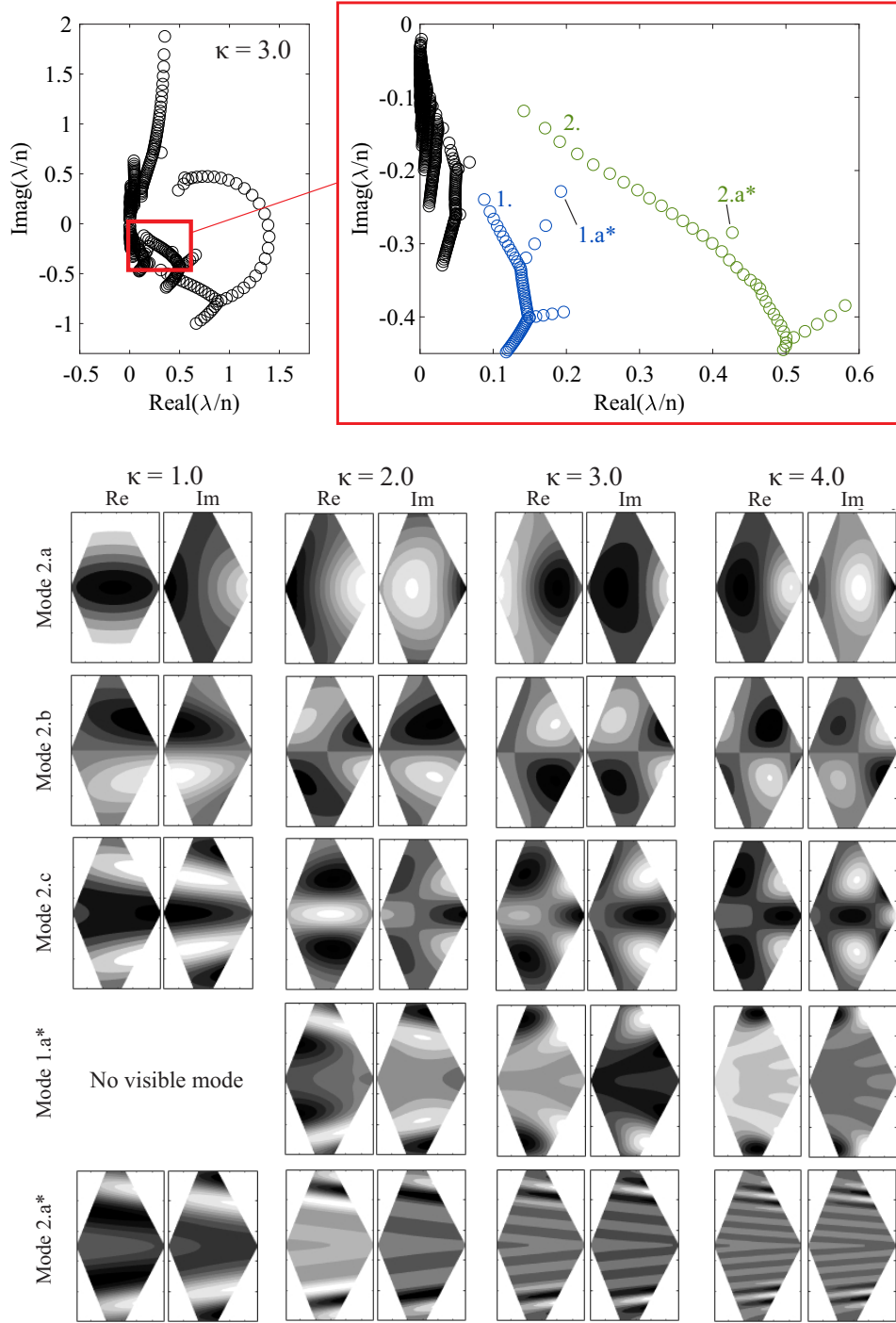


FIG. 16. Eigenvalues and right eigenvectors obtained from the tapered wing geometry. The eigenvalue branches of interest are marked 1 and 2 in the eigenvalue plot, with two modes of special interest being marked 1.a* and 2.a*.

same efficiency as the remaining wings. While their results do not fully support the idea that aspect ratio is unimportant for efficiency, it does bear similarity to the concept of a cut-in frequency beyond which the efficiencies of different geometries are similar.

It is notable that the efficiencies of all eigenmodes from all geometries studied in this paper settle to approximately the

same hydrodynamic efficiency: either around 95% or around 80%, depending on the eigenvalue category. The high efficiency is maintained for increasing κ , which differs from heaving and pitching motion, for which efficiency decreases with increasing κ . Since the eigenmodes in general resemble travelling waves, the most relevant comparison is to the analysis by Wu (1961)²² of 2D waving plates, considering only

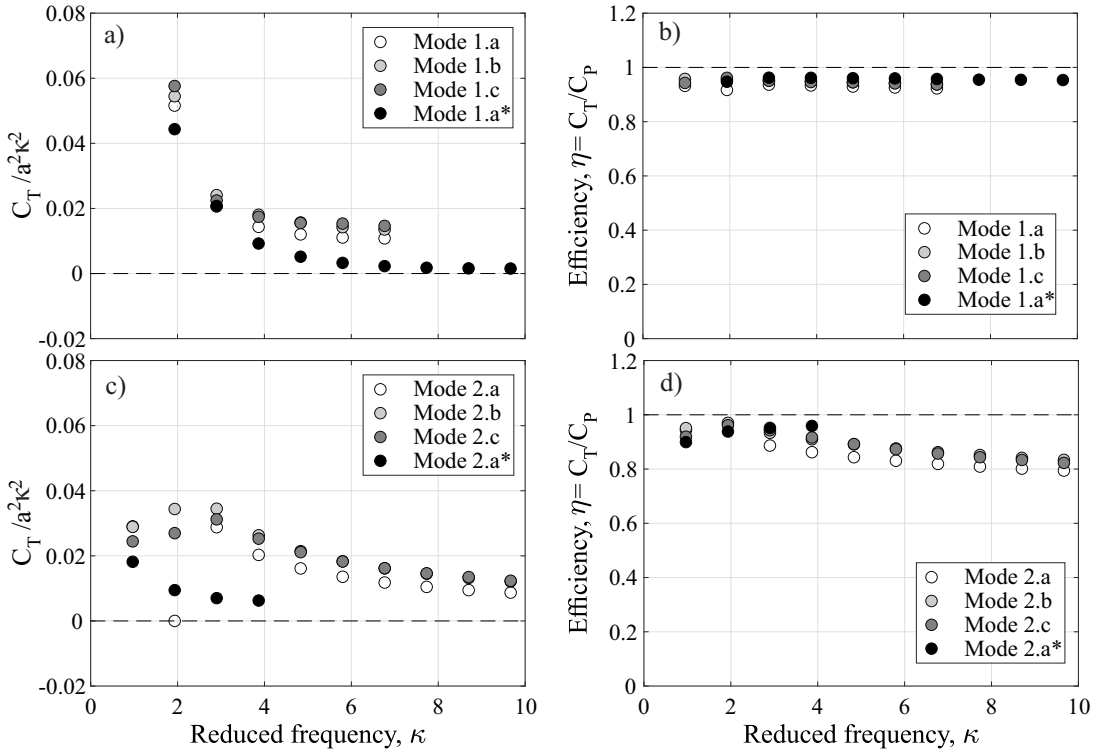


FIG. 17. Propulsive properties against reduced frequency κ for a selection of eigenvectors from the elliptical geometry. The legend notation corresponds to that of Figure 16. a) & d) Normalised thrust, b) & e) Froude efficiency.

added mass forces. Wu found that the propulsive efficiency is 1 for a uniform travelling wave when the wavenumber is equal to the reduced frequency, but zero thrust is generated in this case. The chordwise wavenumbers of the eigenvectors follow this principle: the wavenumber increases with κ in order to maintain the high-efficiency motion (see Figure 9). The eigenvectors do however produce a finite thrust force, and maintains high propulsive efficiency even as the thrust increases. The present method has the benefit of accounting for 3D geometries and circulatory forces.

A remarkable outcome of the eigenmode analysis is the qualitative similarity of some eigenmodes to swimming motions seen in nature, despite the simplicity of the small-amplitude inviscid VLM used in this paper. This is highlighted in Figure 18, showing selected eigenvectors from three geometries. Note that the selection in Figure 18 is based on similarity to swimming seen in marine animals, not on the performance of the mode. Indeed, in some cases the VLM did not find these modes to have good propulsive performance. However, the purpose of the results in Figure 18 is not to provide a validation of the predictive capabilities of the model – the VLM is much too simple for such comparison – but to merely note the presence of modes that exhibit similarities to swimming kinematics seen in nature among the generated kinematics, despite the simplicity of the VLM.

Figure 18a shows a mode from the elliptical geometry and a marine flatworm. Using data presented by Donovan et al. (2006)⁵⁹ to indicate an approximate representative range of reduced frequencies for flatworms swimming in na-

ture, their measurements of the “sea hare” indicate a range of $\kappa = 10.0 - 34.0$ assuming a specimen length of 30cm. Based on this approximation, the eigenvector has been evaluated at $\kappa = 15.0$. Both the eigenvector and the flatworm show undulatory motion concentrated along the spanwise edges, a phenomenon that occurred at high reduced frequencies for the elliptical geometry in Section VI A. It is notable that flatworms observed in nature tend to swim at high reduced frequencies, and also generally exhibit these motion kinematics.

The VLM used in this paper predicted that the eigenmode shown in Figure 18a did not produce thrust. However, this may be due to limitations in the small-amplitude inviscid vortex lattice model used in this study, or the elliptical geometry not being representative enough of flatworms in nature. Further work is needed to increase the complexity of the underlying hydrodynamic model to include e.g. large-amplitude or viscous effects, and to perform more detailed parametric studies of body geometry effects. Both of these developments are outside the scope of the present study, which aims only to outline and demonstrate the eigenmode analysis described in Section II.

All eigenmodes associated with eigenvalues from “branch 2”, for all geometries, show an increase in motion amplitude from the leading to the trailing edge. The motion amplitude becomes more concentrated at the trailing edge as κ increases. This is a feature commonly seen in swimming animals, and the similarity is illustrated in Figure 18b for the elongated plate, comparing the motion pattern of Mode 2.a to that of a sea snake. The similarity

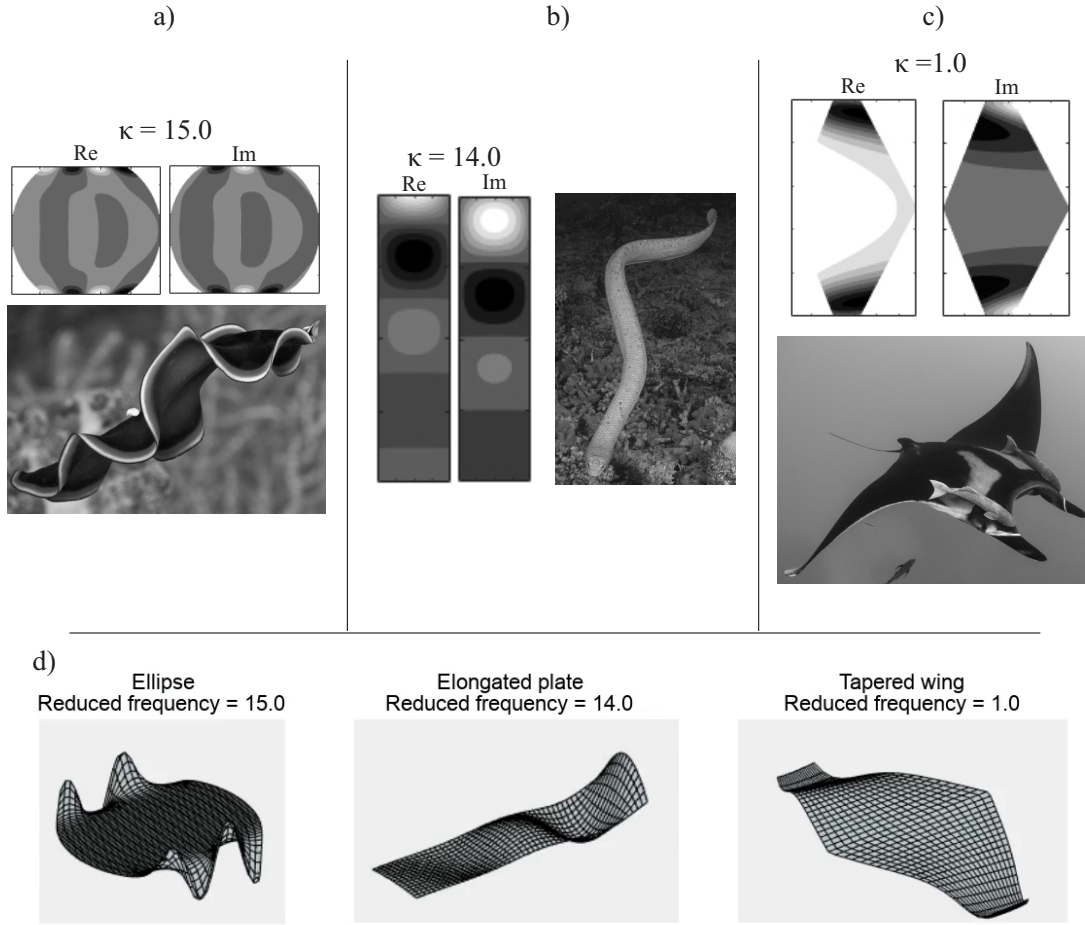


FIG. 18. Qualitative comparison of a selection of eigenvectors with marine animal swimming patterns. a) Ellipse/flatworm (Image credit: The Ocean Agency, stock.adobe.com), b) elongated plate/sea snake (Image credit: The Ocean Agency, stock.adobe.com), c) tapered wing/manta ray (Image credit: Alex Rose, unsplash.com), d) 3D illustrations of the swimming kinematics corresponding to the eigenvectors in a)-c) (multimedia view).

in terms of both wavenumber and the gradual increase of amplitude from leading to trailing edge is notable. The eigenvector is evaluated at $\kappa = 14.0$, which is representative of eel swimming in nature: Tytell and Lauder (2004)⁶⁰ measured $\kappa = 14.18$, Tytell (2004)³² measured $\kappa = 12.24$, and Gillis (1998)⁶¹ measured $\kappa = 15.61$ in their experimental studies of eels at different swimming speeds. Furthermore, Tytell and Lauder (2004)⁶⁰ measured the wavelength of movement to be 0.60 body lengths (wavenumber 1.67), Tytell (2004)³² measured the majority of wavelengths in the range 0.5 – 0.7 body lengths (wavenumber 0.5 – 1.43), and Gillis (1998)⁶¹ measured wavelengths in the range 0.4 – 0.64 body lengths (wavenumber 1.56 – 2.5). Given that the eigenvectors are strongly dependent on κ , the qualitative similarity of the eigenvector in Figure 18b to eel swimming when evaluated at similar κ is striking. Note also that while other modes, such as Mode 3.a in Figure 12, have higher predicted efficiencies than that of Mode 2.a used in Figure 18b, these other modes generally have large leading edge motion amplitudes and are thus liable to cause separation in a viscous flow. This would likely reduce their suitability for swimming kinematics

in favour of Mode 2.a despite its lower inviscid efficiency.

Finally, Figure 18c shows an eigenvector from the tapered wing geometry, in qualitative comparison with a manta ray. The eigenvector has been evaluated at $\kappa = 1.0$, based on a study by Fish et al. (2016)⁶² where the representative swimming speed was set to 1 body length per flapping cycle. The eigenmode kinematics in Figure 18c are oscillatory in the chordwise direction (the wavelength of motion is longer than the chord) and undulatory in the spanwise direction (motion wavelength is shorter than the span), which according to Fish et al. (2016)⁶² is also observed in swimming manta rays.

For 3D visualisation of the swimming kinematics given by the eigenvectors in Figure 18a-c, see Figure 18d (multimedia view). While the present study makes only brief qualitative comparison between eigenmode kinematics and swimming motion found in nature, overall the results visualised in Figure 18 show the potential of hydrodynamic eigenmode decomposition to potentially explore and identify features of efficient swimming motion as observed in marine life.

VIII. CONCLUSIONS

This study has investigated the use of hydrodynamic eigenmodes for generating swimming kinematics resulting in high propulsive (Froude) efficiency, given a 3D body geometry. By assuming a linear system, and using the hydrodynamic eigenvectors as basis functions for the circulation distribution, we have demonstrated that swimming according to a single appropriately selected eigenvector maximises the propulsive efficiency. The analysis was then carried out for a selection of simple geometries, using an inviscid frequency-domain vortex lattice model to represent the hydrodynamic system (more advanced hydrodynamic models can be used in conjunction with the eigenmode analysis, such that the simplicity of the underlying model is not a limitation of the method).

The efficiencies achieved were consistently high for all thrust-producing eigenmodes, with very little variation between the different geometries. Two primary categories of modes were identified; in the first category (modes associated with “eigenvalue branch 2”) the motion amplitude of the associated eigenvector kinematics increased from the leading to trailing edge, similar to the motion pattern of marine animals in nature. In the second category, the motion amplitudes were uniform in the chordwise direction. The Froude efficiency of the former was in the range 70-80%, while the latter was generally 95% or higher (note that these efficiencies are obtained from an inviscid model). This exceeds peak efficiencies achieved by heaving and pitching motion, especially at high frequencies. Changes to aspect ratio or planform had little discernible effect on the maximum achievable efficiency in this study. This suggests that high-efficiency inviscid swimming motion can be achieved irrespective of geometry, by using the kinematics generated using hydrodynamic eigenmode decomposition.

The kinematics generated through the eigenmodes were strongly dependent on reduced frequency κ . The kinematics were generally similar to travelling waves. The chordwise wavenumber of the motion increased with increasing κ , meaning that as κ increased the eigenmodes shifted from producing oscillatory to undulatory motion. The rectangular geometries tested had no change in spanwise wavenumber with increasing κ , while for the two bio-inspired geometries changes to the spanwise wavenumber were often more significant than those to the chordwise. These results suggest that the optimum swimming kinematics for a given body planform will depend strongly on both the 3D geometry and the beat frequency.

Despite the simplicity of the underlying inviscid model used for this study, some of the hydrodynamic eigenmodes bore remarkable similarity to swimming motion seen in nature. While improvements to the underlying hydrodynamic model will make the method more appropriate for real-world applications, the above findings demonstrate the potential of eigenmode analysis for generating high-efficiency swimming kinematics for the study of marine animal gaits or AUV design.

CONFLICTS OF INTEREST

The authors have no conflicts to disclose.

DATA AVAILABILITY STATEMENT

The data that support the findings in this study are available from the corresponding author upon reasonable request.

AUTHOR CONTRIBUTIONS

Amanda S. M. Smyth: Conceptualization (equal); Methodology (supporting); Formal Analysis (lead); Software (lead); Writing/Original Draft Preparation (lead).

Anna M. Young: Conceptualization (equal); Supervision (lead); Writing/Review & Editing (lead).

Luca Di Mare: Conceptualization (equal); Methodology (lead); Writing/Review & Editing (supporting).

Appendix A: Eigenmode analysis including circulatory forces

In Section II B it was demonstrated that the hydrodynamic eigenmodes can be used to generate high-efficiency swimming kinematics if the forces are dominated by added mass. This Appendix demonstrates that the analysis also applies to cases that include circulatory forces.

We retain the notation from Section II B, including expressing time-varying harmonic properties in terms of Fourier components (e.g. $\Gamma(x, y, t) = \hat{\Gamma}(x, y)e^{j\omega t}$). The circulatory forces caused by a surface vorticity distribution can be written as (with subscript c indicating circulatory force components):

$$\frac{\mathbf{F}_c(x, y, t)}{dS} = -\rho \text{Re}[\mathbf{U}_T(x, y, t)] \times \text{Re}[\boldsymbol{\gamma}(x, y, t)] \quad (\text{A1})$$

The total velocity \mathbf{U}_T consists of the freestream velocity \mathbf{U} , body velocity $j\omega\mathbf{h}$ and wake-induced velocity \mathbf{u}_w :

$$\mathbf{U}_T(x, y, t) = \begin{bmatrix} U \\ 0 \\ 0 \end{bmatrix} + e^{j\omega t} \begin{bmatrix} 0 \\ 0 \\ j\omega\hat{\mathbf{h}} + \hat{\mathbf{u}}_w \end{bmatrix} (x, y) \quad (\text{A2})$$

The instantaneous circulatory thrust force is then given by:

$$\begin{aligned} T_c &= \int_S \left[-\frac{\mathbf{F}_c(x, y, t)}{dS} \cdot \mathbf{i} \right] dS \\ &= \rho \int_S \text{Re}[j\omega\mathbf{h}(x, y, t) + \mathbf{u}_w(x, y, t)] \text{Re}[\boldsymbol{\gamma}(x, y, z)] dS \end{aligned} \quad (\text{A3})$$

It can be shown that the resulting cycle-average circulatory force is

$$\bar{T}_c = \frac{\rho}{2} \int_S \{ \omega \text{Im}[\hat{\gamma}^*(x,y)\hat{h}(x,y)] + \text{Re}[\hat{\gamma}^*(x,y)\hat{u}_w(x,y)] \} dS \quad (\text{A4})$$

Circulatory power is given by the inner product of the circulatory force with the transverse body velocity:

$$P_c = \int_S \left[\frac{\mathbf{F}_c(x,y,t)}{dS} \cdot \mathbf{k} \right] \text{Re} \left[\frac{\partial \mathbf{h}(x,y,t)}{\partial t} \cdot \mathbf{k} \right] dS \\ = \rho U \omega \int_S \text{Re}[\gamma(x,y,t)] \text{Re}[jh(x,y,t)] dS \quad (\text{A5})$$

The resulting cycle-average circulatory power can be shown to be

$$\bar{P}_c = \frac{\rho U \omega}{2} \int_S \text{Im}[\hat{\gamma}^*(x,y)\hat{h}(x,y)] dS \quad (\text{A6})$$

Following the definition in Equation 1, we can then define the efficiency of the circulatory forces as follows:

$$\eta_c = \frac{\int_S \{ \omega \text{Im}[\hat{\gamma}^*(x,y)\hat{h}(x,y)] + \text{Re}[\hat{\gamma}^*(x,y)\hat{u}_w(x,y)] \} dS}{\omega \int_S \text{Im}[\hat{\gamma}^*(x,y)\hat{h}(x,y)] dS} \quad (\text{A7})$$

Following the analysis in Section II B for Equation 21, we can approximate the efficiency by defining the surface distributions at discrete points, represented by column vectors. We also note that the wake-induced velocity \hat{u}_w is linearly related to the bound circulation $\hat{\gamma}$ through Equation 29. As such, we can express the wake-induced velocity at each point as

$$\hat{u}_w = \mathcal{A} \hat{\gamma} \quad (\text{A8})$$

where the matrix \mathcal{A} represents the linear transform from the bound vorticity to the wake-induced velocity, given by Equations 27-29. Then we obtain the following:

$$\eta_c \approx \frac{\sum_k \{ \omega \text{Im}[\hat{\gamma}_k^* \hat{h}_k] + \text{Re}[\hat{\gamma}_k^* (\mathcal{A} \hat{\gamma})_k] \} \Delta S}{\omega \sum_k \text{Im}[\hat{\gamma}_k^* \hat{h}_k] \Delta S} \quad (\text{A9})$$

Replicating the method in section II B such that $\hat{\Gamma} = \mathbf{R}\alpha$ and $\hat{h} = \mathbf{R}\beta$, and noting that $\gamma = \partial\Gamma/\partial x$ and that $\alpha = \Lambda^{-1}\beta$, we obtain the following expression:

$$\eta_c \approx 1 + \frac{\sum_k \text{Re}[(\frac{\partial \mathbf{R}}{\partial s} \alpha)_k^* (\mathcal{A} \mathbf{R} \Lambda^{-1} \beta)_k]}{\omega \sum_k \text{Im}[(\frac{\partial \mathbf{R}}{\partial s} \alpha)_k^* (\mathbf{R} \beta)_k]} \quad (\text{A10})$$

This expression shows that the influence of the wake, represented by the numerator in the fraction in Equation A10, is the sole determinant of the circulatory efficiency. Any wake downwash will cause either a reduction in circulatory efficiency from unity (wake damping) or an increase above 1 (wake-induced flutter). We can simplify the expression for wake influence further, in terms of a parameter ϕ such that

$$\mathcal{A} \mathbf{R} \Lambda^{-1} = -j\omega \mathbf{R} \phi \quad (\text{A11})$$

giving the efficiency as:

$$\eta_c \approx 1 - \frac{\sum_k \text{Re}[(\frac{\partial \mathbf{R}}{\partial s} \alpha)_k^* (j\mathbf{R} \phi \beta)_k]}{\sum_k \text{Im}[(\frac{\partial \mathbf{R}}{\partial s} \alpha)_k^* (\mathbf{R} \beta)_k]} \quad (\text{A12})$$

Similar to the role of the parameter ϵ in Equation 25, the circulatory efficiency is then fully determined by the entries in the matrix ϕ , which is given by:

$$\phi = \frac{-1}{j\omega} \mathbf{L} \mathbf{B} \mathcal{A} \mathbf{R} \Lambda^{-1} \quad (\text{A13})$$

As was concluded in Section II B, if only a single entry of β is nonzero, such that the body motion is given by the corresponding eigenvector, then only one entry on the diagonal of ϕ will contribute to the overall efficiency in Equation A12. If N entries of β are nonzero, then $[N \times N]$ entries of ϕ will appear as a sum in the numerator of Equation A12, including both on-and off-diagonal values. Thus it is desirable to choose β to be nonzero only at the single entry that corresponds to the lowest wake influence.

It is not possible to combine ϵ and ϕ , such that a single parameter determines the efficiency of the combined added mass and circulatory forces. It can be demonstrated that the full efficiency is given by:

$$\eta_{m+c} \approx 1 - \frac{\sum_k \left\{ \text{Im}[(\mathbf{R}\alpha)_k^* (j\mathbf{R}\epsilon\beta)_k] - \frac{1}{\kappa} \text{Re}[(\frac{\partial \mathbf{R}}{\partial s} \alpha)_k^* (j\mathbf{R}\phi\beta)_k] \right\}}{\sum_k \left\{ \text{Re}[(\mathbf{R}\alpha)_k^* (\mathbf{R}\beta)_k] - \frac{1}{\kappa} \text{Im}[(\frac{\partial \mathbf{R}}{\partial s} \alpha)_k^* (\mathbf{R}\beta)_k] \right\}} \quad (\text{A14})$$

Thus both ϵ and ϕ determine the overall efficiency, but if the wake influence is low or the reduced frequency κ is large the efficiency can be approximated using the added mass only. It is not straightforward to identify high-efficiency modes by directly studying the ϵ and ϕ matrices. However, it remains the case that it is beneficial to select β to be nonzero only at a single entry, rather than at multiple entries, such that the body motion is given by a single eigenvector. Thus the method of evaluating the efficiency of each individual eigenvector, as adopted in the results sections of this paper, is the most practical way of identifying high-efficiency kinematics from the eigenmodes.

¹M. J. Lighthill, "Aquatic animal propulsion of high hydromechanical efficiency." *Journal of Fluid Mechanics* **44**, 265–301 (1970).

²T. Van Buren, D. Floryan, A. T. Bode-Oke, P. Han, H. Dong, and A. Smits, "Foil shapes for efficient fish-like propulsion." *AIAA Scitech 2019 Forum* (2019).

³K. D. V. Ellenrieder, K. Parker, and J. Soria, "Flow structures behind a heaving and pitching finite-span wing." *Journal of Fluid Mechanics* **490**, 129–138 (2003).

⁴J. M. Anderson, K. Streitlien, D. S. Barrett, and M. S. Triantafyllou, "Oscillating foils of high propulsive efficiency." *Journal of Fluid Mechanics* **360**, 41–72 (1998).

- ⁵N. S. Lagopoulos, G. D. Weymouth, and B. Ganapathisubramani, "Deflected wake interaction of tandem flapping foils." *Journal of Fluid Mechanics* **903**, A9 (2020).
- ⁶H. Dong, R. Mittal, and F. M. Najjar, "Wake topology and hydrodynamic performance of low-aspect-ratio flapping foils." *Journal of Fluid Mechanics* **566**, 309–343 (2006).
- ⁷J. T. King, R. Kumar, and M. A. Green, "Experimental observations of the three-dimensional wake structures and dynamics generated by a rigid, bioinspired pitching panel." *Physical Review Fluids* **3**, 034701 (2018).
- ⁸K. W. Moored, P. A. Dewey, A. J. Smits, and H. Haj-Hariri, "Hydrodynamic wake resonance as an underlying principle of efficient unsteady propulsion." *Journal of Fluid Mechanics* **708**, 329–348 (2012).
- ⁹A. Andersen, T. Bohr, T. Schnipper, and J. H. Walther, "Wake structure and thrust generation of a flapping foil in two-dimensional flow." *Journal of Fluid Mechanics* **812**, R4 (2017).
- ¹⁰S. Alben, "Optimal flexibility of a flapping appendage in an inviscid fluid." *Journal of Fluid Mechanics* **614**, 355–380 (2008).
- ¹¹D. B. Quinn, G. V. Lauder, and A. J. Smits, "Scaling the propulsive performance of heaving flexible panels." *Journal of Fluid Mechanics* **738**, 250–267 (2014).
- ¹²D. B. Quinn, G. V. Lauder, and A. J. Smits, "Maximizing the efficiency of a flexible propulsor using experimental optimization." *Journal of Fluid Mechanics* **767**, 430–448 (2015).
- ¹³D. Floryan and C. W. Rowley, "Clarifying the relationship between efficiency and resonance for flexible inertial swimmers." *Journal of Fluid Mechanics* **853**, 271–300 (2018).
- ¹⁴C. H. White, G. V. Lauder, and H. Bart-Smith, "Tunabot flex: a tuna-inspired robot with body flexibility improves high-performance swimming." *Bioinspiration and Biomimetics* **16**, 026019 (2021).
- ¹⁵M. F. Platzer, K. D. Jones, J. Young, and J. C. S. Lai, "Flapping wing aerodynamics: Progress and challenges." *AIAA Journal* **46**, 2136–2149 (2008).
- ¹⁶M. Saadat, F. E. Fish, A. G. Domel, V. DiSanto, G. V. Lauder, and H. Haj-Hariri, "On the rules for aquatic locomotion." *Physical Review Fluids* **2**, 083102 (2017).
- ¹⁷A. J. Smits, "Undulatory and oscillatory swimming." *J. Fluid Mech.* **874**, P1 (2019).
- ¹⁸M. J. Lighthill, "Note on the swimming of slender fish." *Journal of Fluid Mechanics* **9**, 305–3017 (1960).
- ¹⁹I. Borazjani and F. Sotiropoulos, "On the role of form and kinematics on the hydrodynamics of self-propelled body/caudal fin swimming." *Journal of Experimental Biology* **213**, 89–107 (2010).
- ²⁰M. Sfakiotakis, D. M. Lane, and J. B. C. Davies, "Review of fish swimming modes for aquatic locomotion." *IEEE Journal of Ocean Engineering* **24**, 237–252 (1999).
- ²¹M. J. Lighthill, "Hydromechanics of aquatic animal propulsion." *Annual Review of Fluid Mechanics* **1**, 413–446 (1969).
- ²²T. Y. Wu, "Swimming of a waving plate." *Journal of Fluid Mechanics* **10**, 321–344 (1961).
- ²³T. Y. Wu, "Hydromechanics of swimming propulsion. part 1. swimming of a two-dimensional flexible plate at variable forward speeds in an inviscid fluid." *Journal of Fluid Mechanics* **46**, 337–355 (1971).
- ²⁴M. Hultmark, M. Leftwich, and A. J. Smits, "Flowfield measurements in the wake of a robotic lamprey." *Experiments in Fluids* **43**, 683–690 (2007).
- ²⁵M. Leftwich and A. J. Smits, "Thrust production by a mechanical swimming lamprey." *Experiments in Fluids* **50**, 1349–1355 (2011).
- ²⁶U. Senturk, "Reynolds number scaling of the propulsive performance of a pitching airfoil." *AIAA Journal* **57** (2019).
- ²⁷A. Mivehchi, Q. Zhong, M. Kurt, D. B. Quinn, and K. W. Moored, "Scaling laws for the propulsive performance of a purely pitching foil in ground effect." *Journal of Fluid Mechanics* **919**, R1 (2021).
- ²⁸F. Ayancik, Q. Zhong, D. B. Quinn, A. Brandes, H. Bart-Smith, and K. W. Moored, "Scaling laws for the propulsive performance of three-dimensional pitching propulsors." *Journal of Fluid Mechanics* **871**, 1117–1138 (2019).
- ²⁹J. H. J. Buchholz and A. J. Smits, "The wake structure and thrust performance of a rigid low-aspect-ratio pitching panel." *Journal of Fluid Mechanics* **603**, 331–365 (2008).
- ³⁰G. Li, L. Zhu, and X. Lu, "Numerical studies on locomotion performance of fish-like tail fins." *Journal of Hydrodynamics* **24**, 488–495 (2012).
- ³¹A. N. Zurman-Nasution, B. Ganapathisubramani, and G. D. Weymouth, "Influence of three-dimensionality on propulsive flapping." *Journal of Fluid Mechanics* **886**, A25 (2020).
- ³²E. D. Tytell, "The hydrodynamics of eel swimming i. effect of swimming speed." *Journal of Experimental Biology* **207**, 3265–3279 (2004).
- ³³G. V. Lauder, B. Flammang, and S. Alben, "Passive robotic models of propulsion by the bodies and caudal fins of fish." *Integrative and Comparative Biology* **52**, 576–587 (2012).
- ³⁴T. Van Buren, D. Floryan, and A. Smits, "Scaling and performance of simultaneously heaving and pitching foils." *AIAA Journal* **57**, 3666–3677 (2019).
- ³⁵S. Alben, C. Witt, T. V. Baker, E. Anderson, and G. V. Lauder, "Dynamics of freely swimming flexible foils." *Physics of Fluids* **24**, 051901 (2012).
- ³⁶T. Kambe, "The dynamics of carangiform swimming motions." *Journal of Fluid Mechanics* **87**, 533–560 (1978).
- ³⁷P. W. Webb and R. W. Blake, "Swimming," in *Functional vertebrate morphology*, edited by M. Hildebrand, D. M. Bramble, K. F. Liem, and D. Wake (Harvard University Press, Cambridge, Massachusetts, 1985) pp. 110–128.
- ³⁸K. W. Moored, "Unsteady three-dimensional boundary element method for self-propelled bio-inspired locomotion." *Computers and Fluids* **167**, 324–340 (2018).
- ³⁹F. Ayancik, F. E. Fish, and K. W. Moored, "Three-dimensional scaling laws of cetacean propulsion characterize the hydrodynamic interplay of flukes' shape and kinematics." *Journal of the Royal Society Interface* **17**, 20190655 (2020).
- ⁴⁰G. S. Triantafyllou, M. S. Triantafyllou, and M. A. Grosenbaugh, "Optimal thrust development in oscillating foils with application to fish propulsion." *Journal of Fluids and Structures* **7**, 205–224 (1993).
- ⁴¹P. W. Webb, "Simple physical principles and vertebrate aquatic locomotion." *American Zoologist* **28**, 709–725 (1988).
- ⁴²D. Floryan, T. Van Buren, C. W. Rowley, and A. J. Smits, "Scaling the propulsive performance of heaving and pitching foils." *Journal of Fluid Mechanics* **822**, 386–397 (2017).
- ⁴³C. Mavroyiakoumou and S. Alben, "Eigenmode analysis of membrane stability in inviscid flow." *Physical Review Fluids* **6**, 043901 (2021).
- ⁴⁴K. C. Hall, R. Florea, and P. J. Lanzkron, "A reduced order model of unsteady flows in turbomachinery." *Transactions of the ASME* (1994).
- ⁴⁵K. C. Hall, "Eigenanalysis of unsteady flows about airfoils, cascades, and wings." *AIAA Journal* **32**, 2426–2432 (1994).
- ⁴⁶R. Florea and K. C. Hall, "Eigenmode analysis of unsteady flows about airfoils." *Journal of Computational Physics* **147**, 568–593 (1998).
- ⁴⁷J. Katz and A. Plotkin, "Low-Speed Aerodynamics (2nd ed., Cambridge aerospace series)," (Cambridge University Press, Cambridge, UK, 2001).
- ⁴⁸A. Muñoz-Simón, A. Wynn, and R. Palacios, "Unsteady and three-dimensional aerodynamic effects on wind turbine rotor loads." *AIAA SciTech Forum* (2020).
- ⁴⁹A. S. M. Smyth and A. M. Young, "Three-dimensional unsteady hydrodynamic modelling of tidal turbines," *Proceedings of the European Wave and Tidal Energy Conference (EWTEC)* (2019).
- ⁵⁰S. A. Kinnas and C. Hsin, "Boundary element method for the analysis of the unsteady flow around extreme propeller geometries." *AIAA Journal* **30**, 688–696 (2012).
- ⁵¹Y. Hirato, M. Shen, A. Gopalarathnam, and J. Edwards, "Flow criticality governs leading-edge-vortex initiation on finite wings in unsteady flow." *Journal of Fluid Mechanics* **910**, A1 (2021).
- ⁵²E. Billingsley, M. Ghomm, R. Vasconcellos, and A. Abdelkefi, "Unsteady aerodynamic analysis and effectiveness of bio-inspired flapping wings in v-formation flight," *Proceedings of the Institution of Mechanical Engineers Part G, Journal of Aerospace Engineering* **237**, 402–418 (2023).
- ⁵³K. Hiroaki, K. Sugimoto, K. Hayasaka, and M. Watanabe, "Nonlinear vibration response of a rectangular sheet under harmonic forced excitation in three-dimensional uniform flow: Influence of excitation amplitudes on frequency response," *Journal of Fluids and Structures* **119** (2023).
- ⁵⁴C. Mavroyiakoumou and S. Alben, "Membrane flutter in three-dimensional inviscid flow," *Journal of Fluid Mechanics* **953** (2022).
- ⁵⁵A. S. M. Smyth, A. M. Young, and L. DiMare, "Effect of three-dimensional geometry on harmonic gust-airfoil interaction," *AIAA Journal* **59**, 737–750 (2021).
- ⁵⁶I. E. Garrick, "Propulsion of a flapping and oscillating airfoil," *NACA Report No. 567* (1936).
- ⁵⁷T. M. Faure, K. Roncin, B. Viaud, T. Simonet, and L. Daridon, "Flapping

- wing propulsion: Comparison between discrete vortex method and other models.” *Physics of Fluids* **34**, 034108 (2022).
- ⁵⁸A. N. Zurman-Nasution, B. Ganapathisubramani, and G. D. Weymouth, “Fin sweep angle does not determine flapping propulsive performance.” *Journal of the Royal Society Interface* **18**, 20210174 (2021).
- ⁵⁹D. A. Donovan, S. C. Pennings, and T. H. Carefoot, “Swimming in the sea hare *aplysia brasiliana*: Cost of transport, parapodial morphometry, and swimming behaviour,” *Journal of Experimental Marine Biology and Ecology* **328**, 76–86 (2006).
- ⁶⁰E. D. Tytell and G. V. Lauder, “The hydrodynamics of eel swimming i. wake structure,” *Journal of Experimental Biology* **207**, 1825–1841 (2004).
- ⁶¹G. B. Gillis, “Environmental effects on undulatory locomotion in the american eel *anguilla rostrata*: Kinematics in water and on land,” *The Journal of Experimental Biology* **201**, 949–961 (1998).
- ⁶²F. E. Fish, C. M. Schreiber, K. W. Moored, G. Liu, H. Dong, and H. Bart-Smith, “Hydrodynamic performance of aquatic flapping: Efficiency of underwater flight in the manta.” *Aerospace* **3** (2016).